University of Groningen

Master Thesis

Proprioceptive Encoding in Spiking Neural Networks for Body Pitch Estimation

Author:
Thomas van der Veen (S3488926)

First examiner:
Prof. Dr. Elisabetta Chicca
Second examiner:
Prof. Dr. Volker Dürr

April 18, 2024

Abstract

Robust insect climbing and locomotion requires a sense of body inclination relative to the substrate. Most insects lack dedicated posture sensing organs. Therefore, it is hypothesized that insects integrate high-level parameters, such as body pitch, from proprioceptive signals (sense of body posture). However, specific details for the representation of body posture in the central nervous system (CNS) of insects remain unknown. The objective of this thesis is to address this research gap by mimicking a portion of the stick insect *Carausius morosus'* central nervous and proprioceptive system to estimate body pitch using unrestricted locomotion and climbing data. An existing spiking neural network (SNN) was modified and extended to simulate tactile hair proprioceptors, descending interneurons (joint angle/angular-velocity estimators), movement primitive interneurons (swing/stance classifiers), and posture neurons (body pitch estimator and climbing classifier). Our findings suggest that the position interneuron performed with an error of approximately 5 % Gaussian noise relative to the ground truth, improved from 10 %. The velocity interneuron classification increased in accuracy from 90.4 % to 92.9 % for a novel model and to 95.6 % for a modified model. A key change is the ability to increase the firing rate by up to ten times. Primitive neurons were optimized to an average Matthew's correlation coefficient (MCC) of 0.56 and were found to efficiently encode for swing, stance, or transition phases. The posture neuron estimated body pitch with an average error of approximately 28 % Gaussian noise and the climbing classifier achieved a Matthew's correlation coefficient (MCC) of 0.59. This suggests that proprioceptive information can be effectively processed using a spiking neural network (SNN) to simulate various stages of the proprioceptive system, ultimately estimating whole-body inclination relative to the substrate. Therefore, these results are further evidence that stick insects use proprioceptive feedback to create an internal representation of higher-order parameters, such as body posture. Furthermore, regarding biomimetic robotics, distributed proprioception could sense variability in the substrate and improve the robustness of inclination estimates, for which this thesis could act as a starting point.

Contents

List of Acronyms

SNN spiking neural network
CNS central nervous system
LIF leaky integrate-and-fire
IFB integrate-and-fire-or-burst
AdEx adaptive exponential integrate-and-fire
ODEs ordinary differential equations
RHS right-hand side
DTW dynamic time warping
MCC Matthew's correlation coefficient
TPR true positive rate
TNR true negative rate
FPR false positive rate
TP true positive
TN true negative
FP false positive
FN false negative
PP predicted positive
PN predicted negative
P Positive
N Negative

1 Introduction

Knowledge of body orientation (roll, pitch, yaw)[1] relative to the substrate is essential for robust locomotion and climbing behavior in various animal species. Navigating complex terrain might require an animal to initiate climbing behavior, correct limb position, or adjust locomotion velocity. To achieve this, closed postural feedback loops manipulate motor neurons based on information sensors located throughout the body. Therefore, the postural and motor systems must work closely together [1]. Some high-level control parameters, such as body pitch, considerably influence the functionality of these closed-loop systems. Due to the absence of dedicated posture measurement organs in stick insects, it is hypothesized that body posture is calculated using distributed sensory information from proprioceptive signals in the body [2]. To test this hypothesis, we combined computational methods with low-level joint angle data to mimic a part of the proprioceptive system of the stick insect *Carausius morosus*. With the goal of estimating the insects' body pitch using a biologically inspired approach.

Little research has been done on how circuits at different levels represent the body [3]. However, computational models allow researchers to hypothesize on the structure of neuron pathways. Several models on insect locomotion [4, 5], interlimb coordination [6, 5], descending interneurons [7] and insect proprioceptors [8, 9] have been developed. Notably, a compelling model was developed for mechanosensory neurons known as hair plates, joint angle measuring proprioceptors, found in the folds of insect joints [10]. Furthermore, Gollin and Dürr (2018) [11] used proprioceptive feedback of hair plates to estimate body pitch of the stick insect with spike generators and artificial neural networks. Cohen (2020) [12] expanded on the idea using a spiking neural network (SNN). SNNs are inspired by the temporal dynamics of biological neural systems. By encoding information in the precise timing of discrete spikes and incorporation neuron and synaptic state, SNNs capture temporal patterns and exhibit great biological plausibility [13]. For a recent review of the topic, the reader is referred to the work of Yamazaki et al. (2022) [14].

Cohen (2020) [12] introduced a SNN comprising of four distinct layers. In the first layer, neurons emulate tactile hair dynamics observed by Okada and Toh (2001) [15] in the American cockroach. Building upon this, the second layer integrates the generated spike trains into descending position and velocity interneurons. These neurons encode joint angles and angular velocities in their spike rate, respectively. The third layer, coined the "movement primitive layer", serves as an incidence detector for layer 2. Some neurons within this layer were identified to encode swing/stance phases or transitions, while for others, the function was still unknown. However, the layer functioned poorly and was not sufficiently understood. Furthermore, the last layer estimated body pitch using a regression model instead of another spiking neuron layer. Recognizing the limitations in Cohen's work (2020) [12], the current thesis objective is to reproduce the results and address its shortcomings. Specifically, the aim is to significanly improve the accuracy of the position, velocity and movement primitive layers. Another goal is to replace the posture layer with a spiking neuron layer, estimating body pitch. The network architecture is designed with current biological knowledge in mind. Combined with the inherent biological nature of SNNs, accurate results would further reinforce the hypothesis that stick insects use proprioceptive feedback to internally represent body posture.

The remainder of this thesis is structured as follows: Section 2 provides scientific background information in the form of a brief literary review. Section 3 provides an introduction to the dataset and a detailed explanation of the architecture, describing the methodology layer by layer. In Section 4, the results are outlined for each layer of the network. Section 5 contains a comparative analysis with the relevant scientific literature, exploring the strengths and weaknesses of the proposed network. The paper concludes with Section 6, offering a summary of key findings derived from the study.

2 Literary Research

To design a biologically plausible SNN emulating the proprioceptive system of a stick insect, a thorough understanding of current scientific knowledge is crucial. Therefore, the knowledge developed in this section will form a basis for the design process of the SNN. First, we explore body pitch estimation in animals, leading to the hypothesis that stick insects use information gathered from the proprioceptive system to estimate high-level parameters. Subsequently, we provide a foundational understanding of proprioception and narrow the focus to the hair plate and its dynamics. Finally, we investigate relevant information regarding descending interneurons.

The method used for body pitch estimation varies greatly between animal species [18]. Some aquatic invertebrates, such as crustaceans [19] or mollusks [20], utilize gravity-sensitive receptors (graviceptors) called statocysts to estimate body pitch. This is particularly efficient since gravity is an excellent frame of reference due to its constant strength and direction. In more complex organisms such as humans, mainly the vestibular system (inner ear), but also the proprioceptive system and the visual system allow a person to maintain their balance and spatial orientation [21]. In contrast, insects lack statocysts or a vestibular system. In the

[1] Pitch involves rotation around the y-axis, which is perpendicular to the body's movement, while roll and yaw are rotations around the x and z axes, respectively.

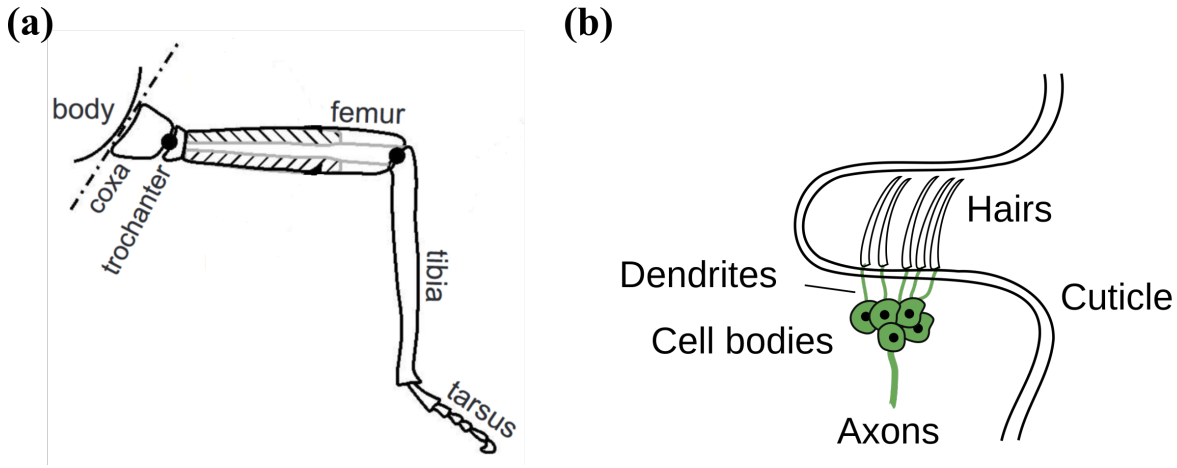

Figure 1: **a.** A schematic of a stick insect's leg. Like other insects, the stick insect possesses six legs characterized by a common morphological structure, consisting of coxa, trochanter, femur, tibia, and tarsus. Adapted from Schneider et al. (2005) [16]. **b.** A cross-sectional schematic of a hair plate. If deflected, the hair applies a force to the tip of the sensory neuron dendrites, initiating the opening of mechanotransduction channels and subsequently generating electrical currents. Adapted from Tuthill and Wilson (2016) [17].

fruitfly *Drosophila melanogaster*, the Johnston's organ's antenna allows for gravity detection due to deflection. If the antenna is ablated, the gravitaxis behavior is reduced but not stopped, suggesting that other posture estimation mechanisms are involved [22]. apart from *Drosophila*, there is a lack of convincing evidence for dedicated posture organs in insects. Therefore, it is hypothesized that ants [23] and stick insects [2] rely on their proprioceptive system to estimate body posture. In this case, body orientation is inferred from the distributed activity of the proprioceptive system.

Proprioception is dependent on groups of mechanosensory neurons spread throughout the body, known collectively as proprioceptors [24, 17]. The information gathered by proprioceptors is sent to the central nervous system (CNS) to form a comprehensive representation of force, self-movement, and body posture [25]. In the context of locomotion, proprioception rectifies limb targeting driven by rythmic central pattern generators in response to disturbances[2]. It also plays a central role in reflexes [27], ensuring precise timing during phase transitions, and regulating the activation timing of individual muscles [24]. Since locomotion is carried out under highly variable conditions, it usually relies partially on sensory input. However, the rapid movements of cockroaches (<20 ms), lead to a predominant dependence on central pattern generators, as the transmission speed of proprioceptive information is insufficient [24]. On the other end of the spectrum, slow moving stick insects have adequate time for proprioceptive feedback to refine locomotion.

Mechanoreceptors can be classified as either rapidly adapting (phasically firing) or slowly adapting (tonically firing) neurons [28]. Slowly adapting neurons encode position, whereas rapidly adapting neurons encode velocity or acceleration (load). In invertebrates, the chordotonal organ measures velocity, and the campaniform sensilla measures load [29, 30]. For a detailed exploration of these proprioceptors, the reader is referred to Tuthill and Azim (2018) [24]. The third element of the invertebrate proprioceptive system involves position sensing performed by hair plates, which will be the primary focus of investigation in this thesis.

Hair plates are typically situated as clusters of individual tactile hairs, or bristles, distributed across the antennae [31], neck [32], and legs [33, 34] of an insect. A cross-sectional schematic of a hair plate is given in figure 1b. In the case of the legs, a common location for hair plates is in the cuticle near the proximal joints, such as the thorax-coxa and coxa-trochanter joints. A schematic of a stick insect leg is given as a reference in Figure 1a. Tactile hairs can be categorized into two types: macrochaetes, and microchaetes, which are longer and shorter in length respectively. Macrochaetes maintain a consistent number and position between individuals within a species, whereas microchaetes display more variability in number, but are generally organized in regularly spaced rows [17, 35, 36]. A tactile hair consists of a hollow hair shaft, anchored at its base to the dendritic tip of a solitary bipolar sensory neuron. If deflected, the hair functions as a lever and applies forces to the tip of the sensory neuron dendrites, initiating the opening of mechanotransduction channels and subsequently generating electrical currents converted into spikes by the sensory neuron[17, 37]. Tactile hairs are directionally selective, and their preferred direction can be predicted from the orientation of the bristle in the cuticle [17]. The function of hair plates may depend on the joint or

[2]In the stick insect, it is hypothesized that each leg has a dedicated step pattern generator [26].

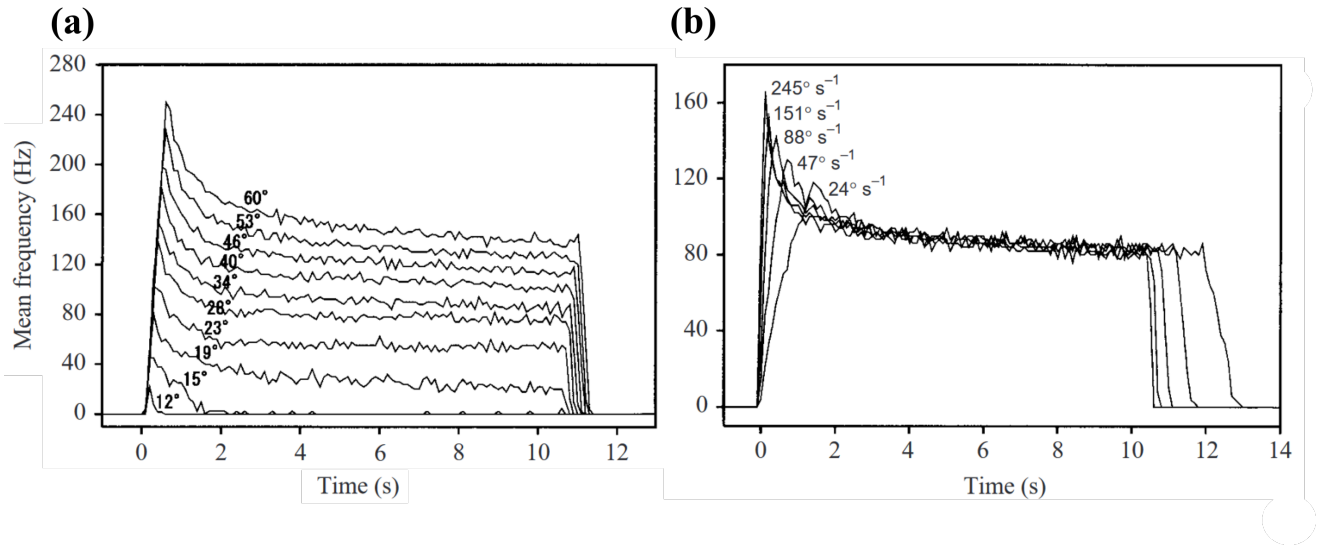

Figure 2: The time courses of spike frequencies for axons of the lateral scapal hair plate in the American cockroach with a sample bin width of 0.1. The frequency is dependent on deflection angle and deflection velocity. **a.** deflection angle is increased from 12° to 60° at a fixed deflection velocity of $60.1\,^\circ\,s^{-1}$. **b.** deflection velocity ($24-245\,^\circ\,s^{-1}$) was varied at a constant angle of 37°. Reprinted from Okada and Toh (2001) [15].

orientation. As an example, trochanter hair plates regulate the animal's height, a critical factor for climbing, as suggested by Burrows (1996) [38]. Additionally, research by Gollin and Dürr (2018) [11] revealed that the middle and hind legs bear greater significance in facilitating climbing behavior. Cruse and Dean (1984) [39] reported that the ventral and dorsal coxal hairplates, the coxal hair rows and the trochanteral hairplate of the middle leg send information to the ipsilateral hind leg to place its tarsus near the tarsus of the middle leg. Showing that proprioceptive feedback is used for inter-leg coordination. Additionally, Hair-plates positioned on the neck (prosternal organ) monitor the head's position relative to the thorax, offering sensory feedback crucial for regulating head posture. In studies involving the blowfly Calliphora, surgical elimination of the prosternal organ hairs on one side led to compensatory head tilting toward the operated side. This suggests the potential involvement of the prosternal organ in gaze stabilization [40].

The individual encoding properties of a single hair were never studied for the stick insect. Electrophysiology recordings exist for the wandering spider *Cupiennius salei* [41], locust [42], and the American cockroach *Periplaneta americana* [15, 34]. Okada and Toh (2001) [15] conducted extracellular recordings from representative sensilla for each subgroup of scapal hair plates. Their study unveiled the distinctive form of single-unit impulses generated in response to hair deflection. They characterized the mechanoreceptor as typically phasic-tonic. Specifically, they observed that the spike frequency during the transient (dynamic) phase was dependent on both velocity and displacement, whereas, in the sustained (steady) phase, it was primarily displacement-dependent. Figure 2 illustrates the time courses of the averaged spike frequencies corresponding to the deflection angle (2a) and the deflection velocity (2b) for a single hair [15], and will form the basis for individual hairs in the computational model of this thesis. These results validate the earlier findings of Pringle (1938) [34] regarding the cockroach trochanter hair plate, except for a significantly higher firing rate ranging from $400-700\,Hz$, in contrast to the $80-240\,Hz$ reported by Okada and Toh (2001).

Afferent sensory information is transferred directly to efferent motor neurons (monosynaptically) or through descending interneurons (polysynaptically), called DINs [43]. Their function include the processing of sensory input, modulation of motor neuron activity, and relaying sensory or proprioceptive information to the brain. Gebhardt and Honegger (2001) [44] identified five DINs in a cricket's antenna, one exhibiting responsiveness to movement and another to the position in the scape-pedicel joint. In the former case, a linear relationship between joint movement and firing frequency was observed. Ache and Dürr (2013) [7] discovered that certain position-sensitive neurons predominantly fire when the antenna is in a dorsal or ventral position. In particular, a study by Mamiya et al. (2018) [45] in the fruit fly *Drosophila*, demonstrated similar joint position encoding, with two DINs firing during flexion or extension and others encoding for bidirectional movement.

The walking leg of a stick insect can be categorized into two distinct states: performing a swing movement or a stance movement. During the stance phase, the leg is in contact with the ground, providing support to the body. In the case of forward walking, the leg moves backward in relation to the body. During the swing

phase, the leg is lifted off the ground and propelled in the direction of walking, preparing for the next stance phase. Stance and swing, are mutually exclusive, indicating that a leg cannot be in both swing and stance simultaneously [46, 47]. In the case of cats [48] and locusts [49], interneurons have been found to fire during the swing or stance phases, or during the transition from swing to stance [49]. However, a notable gap in scientific evidence exists regarding the encoding of body pitch by DINs.

3 Methods

Having established a foundational understanding with a detailed exploration of proprioception, hair plate dynamics, DINs, and body pitch estimation, we are now prepared to translate these insights into the design of the neural network. In this section, we first investigate the stick insect locomotion and climbing dataset. Subsequently, we provide an overview of the overall network architecture, before finally examining each layer in detail. This work is an extension on the work by Cohen. In the remainder of the text, the refererence "Cohen" will simply refer to [12] (2020).

3.1 Dataset

The stick insect has gained scientific prominence due to its slow walking pace, straightforward CNS, and relatively large size. Similar to other insects, the stick insect has six legs characterized by a common morphological structure, comprising coxa, trochanter, femur, tibia, and tarsus. A schematic representation of a stick insect leg is illustrated in Figure 1a. The three pivotal joints include the thorax-coxa joint, which facilitates protraction-retraction movements; the coxa-trochanter joint, which allows levation-depression movements; and the femur-tibia joint, which governs flexion-extension movements [11]. Throughout this thesis, these three joints will be denoted as the α, β, and γ joints, respectively. The front, middle and hind legs are denoted as 1, 2, 3, respectively for the right (R) and left (L) sides. The database used in this study was originally produced to study comparative whole-body kinematics of closely related insect species with different body morphology [50] and characterization of distinct step classes [51]. Furthermore, this data set was used in the body pitch estimation studies of Gollin and Dürr [11] (2018) and Cohen. Gollin and Dürr state in their work: "*This dataset was particularly suitable to investigate body pitch, because the steps of the set-up required transient, large-amplitude adjustment of body pitch. Other parameters could either not be measured accurately (e.g., body roll) or did not vary very much (e.g., body height)*" [11]. For the aforementioned motivations, consistency, and straightforward comparison of results, the same data set was chosen for this study.
The data set comprises complete body kinematics from unrestrained climbing and walking stick insects. Nine specimens freely walked on a horizontal walking path measuring 40 mm in width 490 mm in length. In selected trials, the animals climbed two steps of 48 mm, while others encountered a flat surface. A marker-based motion capture system was employed, using an infrared camera (Vicon MX10) that captures 200 frames per second, to track markers attached to the antenna, legs, and thorax of the insect. These marker trajectories facilitated the reconstruction of joint angle and body pitch time courses during the trials. For each of the six legs, featuring three joints per leg, a total of 18 time courses per trial were captured. [11, 50, 51].

3.2 Network Architecture

The SSN employed in this thesis was adapted from the architecture proposed by Cohen, and is illustrated in Figure 3. The temporal evolution of each joint angle is transformed into a set of hair deflection angles corresponding to the number of hairs in the hair field N_h. Each hair possesses a unique receptive field arranged sequentially with its adjacent hairs. Combining all receptive fields yields sensitivity for the complete angle range of the joint. Each hair deflection is converted into a current which flows into a sensory neuron designated to each hair, subsequently converting the current into spikes. The spike trains for all sensory neurons in a hair plate converge into two position and two velocity DINs. One position interneuron rate encodes joint deflection in the dorsal (posterior relative to rest) position, while the other encodes the ventral position (anterior relative to rest). Similarly, The velocity interneurons encode movement in the forward (dorsal $\rightarrow$ ventral) or backward (ventral $\rightarrow$ dorsal) direction. Each leg of the stick insect has three joints, contains $3 \times N_\mathrm{h}$ sensory neurons, $3 \times 2 = 6$ position interneurons, and $3 \times 2 = 6$ velocity interneurons. The third layer is the movement primitive layer and it consists of 112 primitive movement neurons, each receiving information from two or three position and velocity interneurons within the leg, covering all possible combinations. These neurons function as incidence detectors, triggering a response whenever their inputs coincide. The movement primitive layer is designed to encode leg-specific parameters, capturing aspects like locomotion phases, e.g. when the leg is in swing or stance. Following the movement primitive layer, two posture neurons combine the spike trains generated by the movement primitive layer from all six legs. One posture neuron becomes active during walking, while the other activates during climbing. The combination of these neurons results in a time course for body pitch. There is also a dedicated posture neuron that acts as a binary climbing classifier.

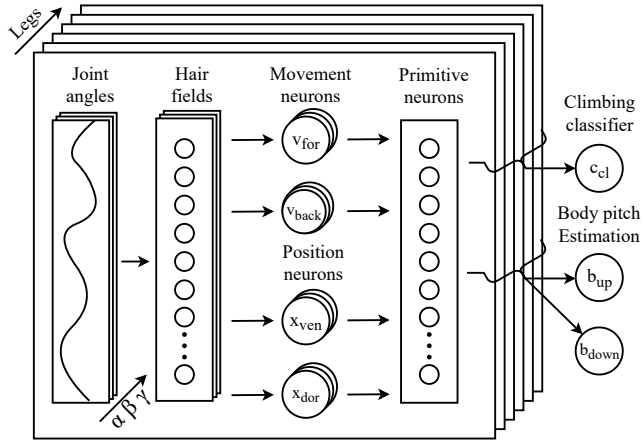

Figure 3: The proposed network architecture consists of four layers: Joint angles are converted into spike trains by the hair field layer. Position and movement neurons transform the combined spike trains into position and movement signals respectively, encoded in the spike rate. Position and movement spike trains are fed to the primitive layer, which acts as an incidence detector. The movement primitive layer combines information from the whole leg and information of all legs is integrated into the climbing classifier, a neuron that fires during insect climbing. Additionally, The posture neurons encode body pitch through rate encoding.

The proposed architecture was implemented directly in Python version 3.9. The simulations were performed on a system with 16 GB RAM and an AMD Ryzen 5600x processor. The differential equations governing neuron and synaptic dynamics were solved using the backward difference method over time, using a time step of $dt = 1\,\text{ms}$.

3.3 Spike Rate

In SNNs, spikes and no spikes are represented as ones and zeros, respectively. A spike train is a sequence of discrete events through time and can be defined as follows [52]:

$$\rho(t) = \sum_{i=1}^{n} \delta(t - t_i), \tag{1}$$

where $\rho(t)$ denotes the spike train, n is the number of spikes, δ is the Dirac delta function, t represents time, and t_i signifies spike times. SNNs often encode information in their firing rates, representing the number of spikes per second. This is calculated as follows [52]:

$$r(t) = \frac{1}{\Delta T} \int_{t-\Delta t/2}^{t+\Delta t/2} \rho(\tau) d\tau. \tag{2}$$

Here, Δt is a time interval. In the Python code, time is discretized with a timestep of dt, and Eq. (2) simplifies to:

$$n = \frac{\Delta T}{dt}, \tag{3}$$

$$r(t_i) = \frac{1}{\Delta T} \sum_{k=t_i-\frac{n}{2}}^{t_i+\frac{n}{2}} \rho(t_k), \tag{4}$$

where n represents the number of steps in ΔT. Due to the nature of the method, edge effects can make results unreliable within $\frac{\Delta T}{2}$ from the edge. In this thesis, $\Delta T = 50\,\text{ms}$, and all spike rates are estimated with this method, unless stated otherwise. Notably, this method diverges from Cohen's approach, where the author utilized the inverse of inter-spike-interval (ISI) as an estimate for spike rate. In principle, all methods are estimates, and results should be interpreted accordingly.

3.4 Layer One: Hair Field Layer

3.4.1 Hair Angles

The time course of each joint angle is transformed into a set of hair deflection angles corresponding to the number of hairs on the hair plate N_h. Each hair features a distinctive receptive field arranged in sequence with its neighboring hairs. A receptive field is defined as the range of joint angles within which the sensilla deflects. The collective contribution of all hairs spans the entire possible range of the joint angle. for the sake of simplicity, it was assumed that the receptive field size and the spacing between hairs are uniform for all hairs within a given hair plate, deviating from the variation observed in biological hair plates [34]. However, a degree of overlap was assumed to be present between receptive fields. This assumption is made since it is unlikely that a full deflection of one hair aligns precisely with the start of deflection for the next hair. Furthermore, it was assumed that the hair deflection was linearly proportional to the joint angle and the range was bound to $[0°, 90°]$. If the joint angle falls below or exceeds the proprioceptor receptive field, the hair angle is considered to be 0° or 90° (no deflection or full deflection), respectively. This yields the following relation between joint angle (θ) and hair angles ($\phi^{(ij)}$):

$$\phi^{(ij)}(\theta) = \begin{cases} 0, & \text{if } \theta < \theta_{\text{rf1}}^{(ij)} \\ 90, & \text{if } \theta > \theta_{\text{rf2}}^{(ij)} \\ \frac{90(\theta - \theta_{\text{rf1}}^{(ij)})}{\theta_{\text{rf2}}^{(ij)} - \theta_{\text{rf1}}^{(ij)}}, & \text{otherwise} \end{cases} \tag{5}$$

where $\theta_{rf1}^{(ij)}$ and $\theta_{rf2}^{(ij)}$ are the receptive field edges for hair i and hair row j and are defined as follows:

$$\theta_{\text{rf1}}^{(ij)} = \frac{\theta_{\text{max}}^{(j)} - \theta_{\text{min}}^{(j)}}{N_\text{h}}(i-1) + \theta_{\text{min}}^{(j)} - \frac{\theta_{\text{overlap}}^{(j)}}{2}, \tag{6}$$

$$\theta_{\text{rf2}}^{(ij)} = \frac{\theta_{\text{max}}^{(j)} - \theta_{\text{min}}^{(j)}}{N_\text{h}} i + \theta_{\text{min}}^{(j)} + \frac{\theta_{\text{overlap}}^{(j)}}{2}, \tag{7}$$

where $\theta^{(j)}_{\text{max}}$ and $\theta^{(j)}_{\text{min}}$ represent the maximum and minimum joint angles for hair row j, respectively. The receptive fields of the outer hairs are set manually: $\theta^{(0j)}_{\text{rf1}} = \theta^{(j)}_{\text{min}}$ and $\theta^{(Nj)}_{\text{rf2}} = \theta^{(j)}_{\text{max}}$. $\theta^{(j)}_{\text{overlap}}$ is a parameter that controls the amount of overlap between receptive fields.

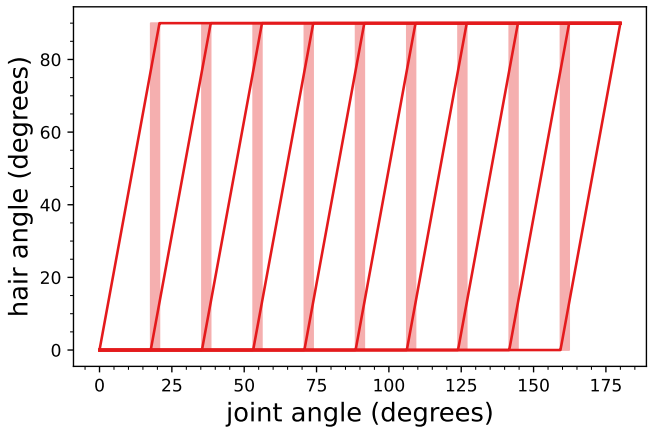

Figure 4: Uni-directional hair plate: hair angle as a function of the joint angle for the hypothetical case where there is a single hair row, $\theta_{\text{min}} = 0°$, $\theta_{\text{max}} = 180°$, $\theta_{\text{overlap}} = 4°$, and $N_{\text{h}} = 10$

Figure 4 illustrates the hair angle as a function of the joint angle in a hypothetical scenario with one hair row, $\theta_{\text{min}} = 0°$, $\theta_{\text{max}} = 180°$, $\theta_{\text{overlap}} = 4°$, and $N_{\text{h}} = 10$. Hair angles increase linearly with joint angle, the shaded region depicts the overlap of neighboring receptive fields.

3.4.2 Sensory Neuron

If a hair is deflected, the mechanotransduction channels open and generate a current. To reflect this, the hair angles were multiplied by $I/\phi = 5 - 37\,\text{nA}\,^{\circ -1}$, which resulted in currents in the nA range. This current runs into a single sensory neuron. To model the sensory neuron, inspiration was drawn from empirical data on the dynamics of mechanosensory neurons characterized by Okada and Toh (2001) [15]. These experiments were conducted on the antenna of the American cockroach *Periplaneta americana*. Therefore, the mechanosensory mechanisms were assumed to be similar between species. Replicating these nonlinear spiking dynamics (Figure 2) was possible for multiple neuron models [53]. However, Cohen opted for the adaptive exponential integrate-and-fire (AdEx) while carefully considering biological plausibility, implementation costs, and potential spiking dynamics [54]. The AdEx model consists of two ordinary differential equations (ODEs):

$$C\frac{dV}{dt} = I - g_{\text{l}}(V - E_{\text{L}}) + g_{\text{l}}\Delta_T exp(\frac{V - V_{\text{T}}}{\Delta_T}) - \omega, \quad (8)$$

$$\tau_\omega \frac{d\omega}{dt} = a(V - E_{\text{l}}) - \omega, \quad (9)$$

where V represents the membrane potential, C denotes the capacitance, I the input current, g_{l} the leak conductance, E_{L} the leak reversal potential, Δ_T is the slope factor, V_{T} the threshold voltage, ω is the adaptation variable, a is the adaptation coupling factor, and τ_ω the adaptation time constant [54]. In a real neuron, an action potential (spike event) occurs due to hyperpolarization. In the AdEx model, when the membrane potential reaches the threshold voltage, a spike is recorded as t^f. the membrane potential resets to the reset voltage V_R and the adaptation variable increases with constant b:

$$if \;\; t = t^f \;\; then \;\; V \rightarrow V_R \;\; and \;\; \omega \rightarrow \omega + b. \quad (10)$$

The second term in Eq. (8) on the right-hand side (RHS) represents the leakage mechanism that allows the membrane voltage to return to E_{L} in the absence of applied current. In a biological neuron, this leakage term represents the random diffusion of ions through the membrane. The third term enables the membrane voltage to exhibit an exponential spike if it surpasses the threshold voltage, leading to depolarization of the membrane potential. The fourth term in the RHS corresponds to the adaptation term, which indicates a gradual decrease over time in the sensitivity of the sensory system to a sustained stimulus. Consequently, an increase in ω results in a decrease in the membrane voltage sensitivity to an input current. The adaptation variable increases when the membrane voltage exceeds its resting state (Eq. (9)) or after a spike event (Eq. (10)). In the absence of spikes, the dynamics described in Eq. (9) facilitate the convergence of the adaptation variable back to zero, resetting the adaptation process.

3.4.3 Replicating Tactile Hair Dynamics

The objective of the AdEx neuron is to replicate the electrophysiological dynamics observed by Okada and Toh (2001) [15], as shown in Figure 2. Cohen utilized the procedures conducted by Okada and Toh (2001) [15] to assess the accuracy of the proposed method. However, these dynamics assume extremely slow angular velocities for the hairs, This lead to a $\tau_\omega = 600\,\text{ms}$ in the work of Cohen. A high value for the time constant leads to significant delays in the velocity and position interneurons, adaptation is still active when it is not desired. Therefore, in this thesis the time constant is is set as $\tau_\omega = 50\,\text{ms}$ and the angular velocities in the procedure are quadrupeled and total time divided by four. With this approach, general dynamics can still be replicated, just not exact timings of the spike rate. The procedures is therefore are as follows [15, 12]:

1. A ramp function was used to linearly increase the deflection of hair sensilla, ranging from 0° to a maximum deflection angle of 37°. The deflection velocity varied with values of $980\,^\circ\,s^{-1}$, $604\,^\circ\,s^{-1}$, $352\,^\circ\,s^{-1}$, $188\,^\circ\,s^{-1}$, and $96\,^\circ\,s^{-1}$.

2. A ramp function that increases linearly at a constant velocity of $240.4\,^\circ\,s^{-1}$ from 0° to varying end angles: 60°, 46°, 34°, 23°, 15°.

The AdEx parameters were initially taken from Cohen's work. A grid search method was employed to vary the values of I/ϕ and b within the ranges of $5\,\text{nA}\,^{\circ -1}$ to $37\,\text{nA}\,^{\circ -1}$ and 50 pV to 350 pV respectively, with a total of 8 steps. In each iteration of the grid search calculation, an error metric was computed to measure the deviation from the dynamics observed in the study by Okada and Toh (2001) [15] for key spike rates (peak and plateau). The error metric is defined as follows:

$$E = \sum_{i}^{10} (\mid \hat{x}^{(i)}_{\text{plat}} - x^{(i)}_{\text{plat}} \mid + \mid \hat{x}^{(i)}_{\text{max}} - x^{(i)}_{\text{max}} \mid), \qquad (11)$$

In the equation above, i represents one of the 10 ramp function trials. $x^{(i)}_{\text{plat}}$ refers to the spike rate at the plateau, $x^{(i)}_{\text{max}}$ represents the maximum spike rate, and the notation $\hat{x}^{(i)}$ indicates values for the AdEx model. On the other hand, the values of $x^{(i)}$ are extracted from the dynamics shown in Figure 2.

3.5 Layer Two: Position Layer

3.5.1 Modified Hair Plate

There is substantial evidence for position encoding in interneurons [7, 45]. To achieve this with SNNs, Cohen, theorized: *"the overall activity of the hair row could be decoded as the joint angle time course by an interneuron that receives information from all proprioceptors in the hair field."* Two distinct methods were employed for this purpose. Initially, a unidirectional method integrated information from a hair row oriented in one direction. However, the bidirectional (second) approach, quickly demonstrated its advantages. Consequently, the focus of this thesis is exclusively on the bidirectional method, which aligns more closely with biological constraints by considering the morphology of the proprioceptive hair field system in stick insects. Unlike the unidirectional hair plate, the bidirectional hair plate featured two subpopulations of hair fields, with opposing directional sensitivity. Each hair field was linked to its respective interneuron, encoding the joint angle for different segments of the joint range and distinct movement directions. The midpoint of the joint range was established as the "resting" angle, wherein minimal spiking activity was elicited from either the hair field or their corresponding interneurons. To allow the hairs to be oriented in both directions, Eq (5) has to be modified as follows:

$$\phi^{(ij)}(\theta) = \begin{cases} 90, & \text{if } \theta < \theta^{(ij)}_{\text{rf1}} \\ 0, & \text{if } \theta > \theta^{(ij)}_{\text{rf2}} \\ 90\left(1 - \frac{\theta - \theta^{(ij)}_{\text{rf1}}}{\theta^{(ij)}_{\text{rf2}} - \theta^{(ij)}_{\text{rf1}}}\right). & \text{otherwise} \end{cases} \qquad (12)$$

The receptive field edges calculated using Eq. (6) and Eq. (7) are flipped, meaning that the calculations for $\theta^{(ij)}_{\text{rf1}}$ and $\theta^{(ij)}_{\text{rf2}}$ are interchanged.

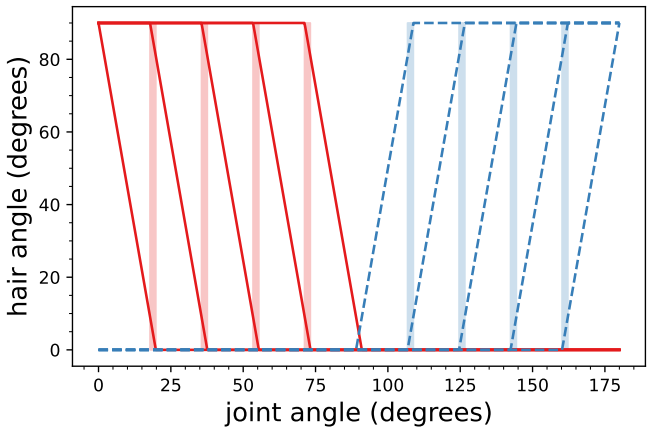

Figure 5: Bidirectional hair plate: Hair angle as a function of the joint angle for the hypothetical scenario where $\theta^{(2)}_{\text{min}} = 88°$, $\theta^{(2)}_{\text{max}} = 180°$, $\theta^{(2)}_{\text{overlap}} = 4°$, and $N^{(2)}_{\text{h}} = 5$ (ventral position in dashed blue) and $\theta^{(1)}_{\text{min}} = 0°$, $\theta^{(1)}_{\text{max}} = 92°$, $\theta^{(1)}_{\text{overlap}} = 4°$, and $N^{(1)}_{\text{h}} = 5$ (dorsal position in solid red). The ventral and dorsal oriented hairs are calculated using Eq (5) and Eq (12) respectively.

Figure 5 shows hair angles as a function of the joint angles for a hypothetical scenario to serve as a visual example. The parameters for the ventral position hair field (dashed blue) are $\theta^{(2)}_{\text{min}} = 88°$, $\theta^{(2)}_{\text{max}} = 180°$, $\theta^{(1)}_{\text{overlap}} = 4°$, and $N^{(2)}_{\text{h}} = 5$. The parameters for dorsal position hair field (solid red) are $\theta^{(1)}_{\text{min}} = 0°$, $\theta^{(1)}_{\text{max}} = 92°$, $\theta^{(1)}_{\text{overlap}} = 4°$, and $N^{(1)}_{\text{h}} = 5$. The calculations for ventral and dorsal oriented hairs are determined using Eq. (5) and Eq. (12), respectively. The ventral oriented hair field is sensitive from $88° \rightarrow 180°$ while the dorsal oriented hair field is sensitive from $92° \rightarrow 0°$. Incorporating an overlap into the hair plate was intended to maintain low but non-zero spike rates at the resting position for the hair field and consequently the interneurons. The overlap between the hair fields (θ_{ohf}) at the resting position (90° in the hypothetical scenario) is defined as follows:

$$\theta_{\text{ohf}} = \theta^{(1)}_{\text{max}} - \theta^{(2)}_{\text{min}} = 92° - 88° = 4°. \qquad (13)$$

3.5.2 Position Interneurons

Due to the nature of the bidirectional hair plate, two interneurons were necessary. The ventral interneuron was connected to the ventral hair field and the dorsal interneuron was connected to the dorsal hair field. Each connection was a synapse, converting sensory spike trains into electrical currents. Cohen chose a synaptic model to mirror the phenomenon observed in the nervous system, whereby a pre-synaptic spike induces depolarization of the post-synaptic neuron's membrane potential. This phenomenon, known as excitatory postsynaptic potential (EPSP), manifests as a swift onset of depolarization reaching a peak, succeeded by a gradual decay. Similar to patterns observed by Sayer et al. [55] (1990). To achieve these dynamics, the synapse is governed by two ODEs [12]:

$$\frac{dW}{dt} = \frac{-W}{\tau_w}, \tag{14}$$

$$\frac{dEPSP_i}{dt} = \frac{W - EPSP_i}{\tau_{EPSP}}, \tag{15}$$

where τ_w and τ_{EPSP} are time constants. After a presynaptic spike, a fixed value c is added to W:

$$if \;\; t = t^f \;\; then \;\; W \rightarrow W + c. \tag{16}$$

After a pre-synaptic spike, the parameter W undergoes an instantaneous increase followed by immediate decay. Consequently, the excitatory postsynaptic potential ($EPSP_i$) rapidly ascends until $W = EPSP_i$, after which it gradually diminishes. All the synapses of a hair field converge at the interneuron, yielding a combined $EPSP$:

$$EPSP = \sum_{i=1}^{N_\mathrm{h}} EPSP_i. \tag{17}$$

EPSP is added to the membrane potential of a modified leaky integrate-and-fire (LIF) model. Like the AdEx model, the LIF model incorporates a "leaky" term, in contrast to its ideal counterpart, the non-LIF model. Apart from the leakage term, the model is extremely simple. It is one of the most popular neuron models available, dating back to Lapicque in 1907 before the generation of neuron action potentials was even understood [56]. Cohen chose the LIF model due to its simplicity and small parameter set, the dynamics emerge from a single equation:

$$\frac{dV}{dt} = \frac{EPSP - (V - V_R)}{\tau}, \tag{18}$$

where V is the neuron membrane potential and τ is the time constant. Like in the AdEx model, if the membrane voltage is greater than the threshold voltage V_T, it is reset:

$$if \;\; t = t^f \;\; then \;\; V \rightarrow V_R \tag{19}$$

3.5.3 Optimization

The objective of the position interneuron is to encode the joint angle time course in its spike rate. To quantify accuracy, an appropriate statistical method is necessary to estimate similarity in time series. dynamic time warping (DTW) is a powerful technique designed to compare two (temporal) sequences, particularly when they lack perfect synchronization. DTW operates by iteratively computing the Euclidean distance between the corresponding points in two temporal arrays. frequently implemented in diverse fields such as speech recognition, data mining, and financial analysis, its utility is well established. For a more comprehensive explanation of DTW methodology, the reader is referred to a review by Senin (2008) [57].

The dataset is sampled at 200 Hz, corresponding to a timestep of $dt = 5$ ms, whereas the SNN network operates with a timestep of $dt = 1$ ms. Hence, the experimental time series need to be interpolated to match the finer timestep. Furthermore, prior to integration into the proprioceptive system, the interpolated time series undergo Gaussian filtering. The time course of the dorsal position interneuron is subtracted from that of the ventral neuron. This methodology diverges from that of Cohen, who solely compared the time course of a single interneuron. Subsequently, the time series are Z-normalized before the DTW procedure. Given the relativistic interpretation of the DTW scores, the initial results are compared against the DTW value between the experimental data and itself with 1 %, 5 % and 10 % Gaussian noise added.

Two synaptic parameters were varied using a grid search approach to minimize the DTW score. The parameters τ_W and b were chosen due to their distinct roles in synaptic decay and strength, respectively. τ_W was swept across a range from 3 ms to 18 ms, while b ranged from 1 mV to 16 mV, each with 4 steps. This method enabled the optimization and verification of network performance by exploring the parameter space.

3.6 Layer Two: Movement Layer

There is scientific evidence for joint movement encoding interneurons [44], and they are crucial in the proprioceptive system. Therefore, the objective of this layer was to construct dependable interneurons capable of conveying accurate information regarding the direction of joint movement. To create such a neuron, certain conditions had to be met. First, the rate at which the neuron fired could not be negative, in the case of backward joint movement. To solve this, two velocity interneurons were needed: one connected to the ventral-oriented hair row (dorsal $\rightarrow$ ventral) and the other to the dorsal-oriented hair row (ventral $\rightarrow$ dorsal). Moreover, if the joint angle was constant, the neurons should not fire. Lastly, the firing rate should increase linearly with the joint velocity. These conditions were already stated by Cohen.

However, this thesis introduced another requirement: the firing rate should be adjustable regardless of the number of sensory hairs. This was necessary for layer three (movement primitive layer) to function properly. With these requirements in mind, consulting Izhikevich (2004) [53] led to the adoption of an integrate-and-fire-or-burst (IFB) neuron model instead of the LIF suggested by Cohen. Combined with inhibitory synapses, the velocity interneurons fired a preset amount of times whenever the joint angle moved from a receptive field to the next, satisfying all the requirements. Furthermore, another model was proposed featuring a contrasting approach. In this model, each sensory neuron was linked to a high-pass filter, selectively firing only during the phasic response. Subsequently, the filtered spikes from all sensory neurons were combined and encoded joint velocity through their combined spike rate.

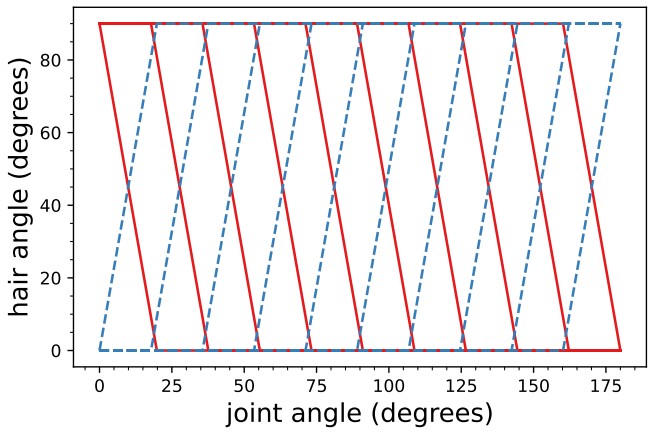

Figure 6: Hair angles as a function of the joint angle. The hypothetical case is modified from Figure 5 as follows: $N^{(1)}_{\text{hairs}} = N^{(2)}_{\text{hairs}} = 10$, $\theta^{(1)}_{\text{max}} = 180°$ and $\theta^{(2)}_{\text{min}} = 0°$, overlap surfaces have been omitted for clarity

3.6.1 Modified Hair plate

Similarly to the position interneuron layer, the movement layer features two velocity interneurons per joint. However, both neurons require sensitivity throughout the range of the whole joint to function properly. Consequently, the hypothetical scenario outlined in Section 3.5.2 was updated by introducing 5 additional hairs and expanding the joint range for both hair fields: $N^{(1)}_h = N^{(2)}_h = 10$, $\theta^{(1)}_{max} = 180°$, and $\theta^{(2)}_{max} = 0°$. This modification results in the (final) hair plate depicted in figure 6, overlap surfaces have been omitted for clarity. The hair field includes all hairs from Figure 5, with the inclusion of 5 additional hairs. Notably, these added hairs were not linked to the position interneuron. There exists no experimental basis for their presence, these hairs are added out of necessity for the movement layer to operate effectively.

3.6.2 Modified Model

The velocity interneuron encodes changes in joint angle by firing whenever the joint angle moves from one receptive field to another. However, sensory neurons operating at lower joint angles continue to fire at their maximum rate because their corresponding hairs are still deflected maximally. This implies that the connection between a sensory neuron and a velocity interneuron should be suppressed after a single spike, requiring self-suppressive synapses. Therefore, each synapse between proprioceptive sensory neuron and velocity interneuron was governed by the following equation:

$$\frac{dG}{dt} = \frac{G_r - G}{\tau_G}, \tag{20}$$

where G is the synaptic weight, G_r is the maximum synaptic strength and τ_G is the synaptic time constant. At each presynaptic spike, the postsynaptic membrane voltage V is increased by the synaptic weight G and the synaptic weight is inhibited as follows:

$$V = V + G, \tag{21}$$
$$G = pG, \tag{22}$$

where p is the inhibition rate. If p is low, inhibition is strong and the membrane voltage is increased very little after the initial presynaptic spike.

In their work, Smith et al. (2000) [58] introduced a new variation of the traditional integrate-and-fire dynamics. They incorporated a gating variable, denoted as h, which represents the presence of a slow Ca^{2+} current. This slow current, also known as the T-channel current, influences the generation of impulse bursts in cells that are recovering from hyperpolarization [59]. Thalamic cells that reach a sufficient level of depolarization do not exhibit bursting behavior, but instead display the typical integration-and-fire behavior when subjected to a depolarizing current. These characteristics have been integrated into the IFB model, which extends the simplified LIF model proposed by Cohen. [12, 58]:

$$\frac{dV}{dt} = -\frac{(V - V_{\text{R}})}{\tau_{\text{l}}} - \frac{m_\infty h(V - V_{\text{T}})}{\tau_{\text{b}}} \tag{23}$$

where the τ_{l} and τ_{b} are the leak and burst time constants respectively, h is the gating variable and $m_\infty(V)$ is an activation function for the Ca^{2+} channels, and is defined as follows [58]:

$$m_\infty(V) = H(V - V_{\text{h}}) = \begin{cases} 1, & \text{if } (V \geq V_{\text{h}}) \\ 0, & \text{if } (V < V_{\text{h}}) \end{cases} \tag{24}$$

where H is the Heaviside step function. The parameter V_{h} divides the V axis into two segments: a hyperpolarizing segment (where $V < V_{\text{h}}$), which is marked by the presence of a deinactivated calcium current. And a non-hyperpolarizing segment (where $V > V_{\text{h}}$), where

the calcium current is inactivated [60]. The gating variable dynamics are given in the IFB model by [58]:

$$\begin{cases} -\frac{h}{\tau_{\mathrm{h}}^{-}}, & \text{if } (V > V_{\mathrm{h}}) \\ \frac{1-h}{\tau_{\mathrm{h}}^{+}}, & \text{if } (V < V_{\mathrm{h}}) \end{cases} \tag{25}$$

the gating variable h tends to converge toward zero or one. The time scale τ_{h}^{-} determines how long a burst event lasts, while τ_{h}^{+} controls the rate at which inactivation occurs [60].

If a postsynaptic spike occurs, the membrane voltage resets to V_{h}, not V_{r}:

$$if \;\; t = t^{f} \;\; then \;\; V \rightarrow V_{\mathrm{h}}. \tag{26}$$

If the membrane voltage resets to V_{h}, Eq. (24) remains equal to one. The neuron will continue to fire until the gating voltage dynamics described by Eq. (25) bring the value of h below a critical threshold, at which point bursting stops.

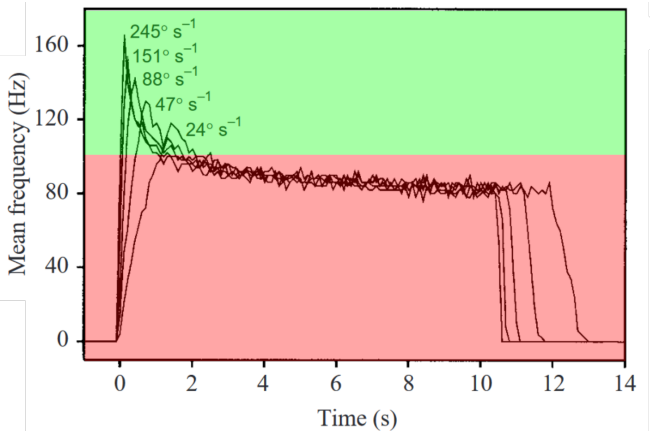

Figure 7: Tactile hair response to a ramp and hold function, a phasic-tonic response. When the signal undergoes high-pass filtering, low frequencies (tonic, red) are attenuated, leaving the high frequencies (phasic, green) intact. In this example, $f_{\mathrm{c}} = 90\,\mathrm{Hz}$. Adapted from Okada and Toh (2001) [15]

3.6.3 Novel Model

The second model exploited the phasic-tonic behavior of the sensory neuron. Figure 7 illustrated the dynamics of the sensory neuron in response to a ramp and hold input. The spike rate peaked and reached a steady state due to adaptation. In the model, the maximum hair deflection angle was always 90°, ensuring that the steady-state firing rate remained constant. By connecting the sensory neuron to a high-pass filter, the steady-state spikes were attenuated while the peak spikes passed through. Figure 7 depicts the attenuated and non-attenuated spikes in red and green respectively, the high pass filter attenuated spikes occuring under 90 Hz. In this way, the high-pass filter only spiked whenever adaptation was low, indicating movement from one receptive field to the next. By combining the spikes of all high-pass filters, a joint angle velocity time course could be constructed.

A high-pass filter is simply constructed from a LIF neuron. A pre-synaptic spike from layer two increased the post-synaptic membrane voltage of the movement primitive neuron by a weight ω:

$$if \;\; t = t^{pre} \;\; then \;\; V = V + \omega. \tag{27}$$

The dynamics of the simplified LIF was as follows:

$$\frac{dV}{dt} = -\frac{(V - V_r)}{\tau}. \tag{28}$$

If the voltage V was larger than the threshold voltage, a spike was recorded as t^{f} and the voltage was reset to V_{R}:

$$if \;\; t = t^{f} \;\; then \;\; V \rightarrow V_{\mathrm{R}}, \tag{29}$$

by tuning ω, f_{c} can be set to the desired value.

3.6.4 Optimization

For the movement layer, various parameters must be configured for both the synaptic and neuron model. Due to several constraints, many of these parameters can be reasonably set using logical arguments, which will be detailed in Section 4.3. To gauge the precision of the model, we assume that the system functions as a binary classifier. The forward oriented movement neuron spikes during forward and backward movements (increasing and decreasing joint angles) are denoted as true positive (TP) and false positive (FP), respectively. Similarly, backward neuron spikes during forward and backward movements are labeled as false negative (FN) and true negative (TN), respectively. Since the number of Positive (P) and Negative (N) occurences is expected to be fairly balanced and symmetric, a simple accuracy calculation suffices:

$$\begin{aligned} TPR &= \frac{TP}{TP + FN}, \\ TNR &= \frac{TN}{TN + FP}, \\ ACC &= \frac{TPR + TNR}{2}, \end{aligned} \tag{30}$$

where the true positive rate (TPR) is the sensitivity and the true negative rate (TNR) is the specificity. An accuracy of zero indicates that all spikes are at the wrong time, and an accuracy of one implies that all spikes occur at the correct timing.

As spikes occur during the transition between sensory receptive fields, the quantity of receptive fields, and consequently, the number of hairs N_{h} in the hair field, has a direct impact on the spike rate. It is anticipated that the spike rate will have a linear increase with the number of hairs. Additionally, the parameter τ_{h}^{-} dictates the duration of a burst event, thereby influencing the spike rate. For the novel velocity model, the parameter ω shifts the cutoff frequency f_c up or down, controlling spike rate. Given the importance of spike rate

control for the subsequent layer, we will experimentally assess the linearity of the spike rate as a function of joint velocity. In addition, the parameters N_{h}, τ_h^+ (modified model) and ω (novel model) are varied to observe their effects on the spike rate.

Finally, the velocity time courses of the movement layer are compared to the velocity time course of the simulations. The discrete joint velocity ($\dot{\theta}$) at timestep t_i is calculated as follows:

$$\dot{\theta}(t_i) = \frac{\theta(t_{i+1}) - \theta(t_i)}{dt}. \tag{31}$$

3.7 Layer Three: Movement Primitive Layer

3.7.1 Synapse Connections

Layer two consisted of two position interneurons and two velocity interneurons per joint. Each leg had three joints, so 12 interneurons per leg. The design of layer three was based on the concept that different combinations of information from the interneurons of different joints could encode various leg actions, e.g. swing and stance phases. Therefore, layer three acted as an incidence detector, each neuron fires only when inputs from two or three joints coincide. This design ensures activation only when there is temporal alignment between the relevant interneurons in the second layer.

Each movement primitive neuron is supplied with input from two or three joints. Specifically, each joint contributes input from one of the layer two interneurons, including the ventral position interneuron (pos_+), dorsal position interneuron (pos_-), forward velocity interneuron (vel_+) and backward velocity interneuron (vel_-) or none (no connection). The previously mentioned interneurons can be combined in a set, e.g. for joint α: $A = \{pos_+^\alpha,\ pos_-^\alpha,\ vel_+^\alpha,\ vel_-^\alpha,\ None\}$ and analogously for joints β and γ as B and C, respectively. To get all possible combinations we perform a 3-fold Cartesian product (denoted by $\times$) of the sets A, B, and C. This results in a set of ordered pairs (a, b, c), where a, b, and c are in A, B, and C respectively, expressed in set builder notation as [61]:

$$D = A \times B \times C = \{(a, b, c) \mid a \in A, b \in B, c \in C\}. \tag{32}$$

This procedure produces a set of $5^3 = 125$ ordered pairs that represent all the possible connections between layers two and three. pairs with more than one $None$ are excluded, (only ordered pairs with two or more active connections are valid), resulting in a final count of 112 ordered pairs in set D. The set naturally groups into seven subsets; the first five were present in the work of Cohen, the last two were added in this thesis:

- $E_1 = \{a \mid a \in D : 2 \times pos, 1 \times None\}$,
- $E_2 = \{a \mid a \in D : 2 \times vel, 1 \times None\}$,
- $E_3 = \{a \mid a \in D : 1 \times pos, 1 \times vel, 1 \times None\}$,
- $E_4 = \{a \mid a \in D : 2 \times pos, 1 \times vel\}$,
- $E_5 = \{a \mid a \in D : 2 \times vel, 1 \times pos\}$,
- $E_6 = \{a \mid a \in D : 3 \times pos\}$,
- $E_7 = \{a \mid a \in D : 3 \times vel\}$,

pos represents either pos_- or pos_+, and similarly, vel represents vel_- or vel_+. In an ordered pair, the first element corresponds to the contribution of joint α, the second to joint β, and so forth. Therefore, the angle superscripts (e.g. $()^\alpha$) are omitted. As an example, the subset E_3 includes the ordered pair (pos_+, vel_+, $None$) or ($None$, pos_-, vel_+), where joint α has no contribution, joint β contributes spikes from the dorsal interneuron, and joint γ contributes spikes from the forward velocity interneuron. The subsets E_1 through E_7 are represented by: p-p, v-v, p-v, p-p-v, v-v-p, p-p-p and v-v-v, respectively. For each ordered pair, there is a corresponding movement primitive neuron. Therefore, there is a total of 672 neurons in total, 112 neurons for six legs.

3.7.2 Synaptic and Neuron Model

In the preceding section, the connections between layer two and layer three were defined. It was clarified that a movement primitive neuron fired whenever the input spikes overlapped closely in time. To achieve this, the neuron functioned as an incidence detector. With this objective in mind, a simplified LIF and simple synapse were found to be sufficient. A pre-synaptic spike from layer two increased the post-synaptic membrane voltage of the movement primitive neuron by a weight ω:

$$if\ \ t = t^f\ \ then\ \ V = V + \omega. \tag{33}$$

The dynamics of the simplified LIF was as follows:

$$\frac{dV}{dt} = -\frac{(V - V_{\mathrm{R}})}{\tau}. \tag{34}$$

If the voltage V was larger than the threshold voltage, a spike was recorded as t^f and the voltage was reset to V_{R}:

$$if\ \ t = t^f\ \ then\ \ V \to V_{\mathrm{R}}. \tag{35}$$

3.7.3 Parameter Optimization

The parameter τ dictated the duration during which the incoming spikes were considered to be in close proximity. Setting τ relatively high could result in spikes that were distant in time triggering a response, potentially leading to a loss of accuracy. On the contrary, if τ was too low, fewer overlapping spikes occurred within the designated time frame, resulting in a lower spike rate for the movement primitive neuron, potentially causing it to not fire when it should. Therefore, optimizing the time constant τ was necessary to achieve maximum accuracy.

Another optimized parameter was the synaptic weight ω, which determined the strength of the synapse. If the synaptic weight was too low, no spikes occurred. On the contrary, if the weight was too high, subsequent spikes from one input might trigger a response. Ideally, a spike from one input would set the membrane voltage close to the threshold. Then, when another spike arrived close in time, the membrane voltage would surpass the threshold voltage. Another aspect considered was the disparity in spiking dynamics between the position and velocity interneurons. Cohen observed that the spiking rate of the position interneuron was significantly higher than that of the velocity interneuron. To address this discrepancy, the author adjusted the synaptic weights of the position to the primitive neuron ($\omega_{textpos}$) to be lower than those of the velocity to primitive neuron (ω_{vel}). In this work, the velocity interneuron was modified or completely replaced to allow flexibility in the spike rate. However, the dynamics were still not equal, so it was useful to separately optimize the synaptic weights ($\omega_{textpos}$) and ($\omega_{textvel}$). Additionally, different combinations of velocity and position interneurons might have varying optimal weight requirements. Especially in the case between two and three inputs. When the weights of two inputs were applied to the situation with three inputs, the primitive neuron spiked when only two inputs overlapped instead of all three. Consequently, for three inputs, the optimal weights are lower than in the case of two inputs.

To account for these multiple variables, the synaptic weights $\omega_{textpos}$ and $\omega_{textvel}$ were individually optimized for the subsets E_1 through E_7, outlined in Section 3.7.1. The accuracy was assessed for each subset while varying $\omega_{textpos}$, $\omega_{textvel}$ and τ. Consequently, each subset had its unique optimal values for $\omega_{textpos}$ and $\omega_{textvel}$ at different values of τ.

For accuracy evaluation, all primitive neuron time courses (predicted condition) were split into 100 uniformly spaced bins. A bin was labeled as predicted positive (PP) if the primitive neuron spiked at least once during the bin, and predicted negative (PN) if no spike occurred. To compare these results, the real joint angles (actual condition) underwent preprocessing to align with the network's framework: pos_+ and vel_+ were categorized as P if the joint was in the ventral position or moving in the forward direction respectively, and N when they were not. Analogous categorization was applied to pos_- and vel_- for dorsal positions and backward motion. Similarly to the predicted condition, these results were binned in 100 equally sized bins.

With both the model estimation and the ground truth binned, predicted and actual conditions were compared by constructing a confusion matrix: counting the TPs, TNs, FPs and FNs. Due to an expected imbalance between P and N occurrences, the traditional accuracy estimation (Eq. (30)) was deemed unreliable. A more suitable metric was found to be the Matthew's correlation coefficient (MCC), a measure of the quality of binary (two-class) classifications [62]. Chicco and Jurman (2020) [63] found that MCC was a more reliable statistical measure than the F1 score and accuracy, producing a high score only if the prediction achieved good results in all four categories of the confusion matrix (TP, FN, TN and FP), proportionally to both the size of positive elements and the size of negative elements in the data set. Its interpretation was closely related to Pearson's correlation coefficient: -1 indicated total negative correlation, 0 did not indicate correlation, and 1 indicated total positive correlation [64]. The MCC was given by [62]:

$$\begin{aligned} N &= TP + TN + FP + FN, \\ S &= \frac{TP + TN}{N}, \\ P &= \frac{FP + FN}{N}, \\ MCC &= \frac{TP/N - S \times P}{\sqrt{PS(1-S)(1-P)}}, \end{aligned} \tag{36}$$

where N is total number of observations, S is the ratio of true observations and P is the ratio of false observations, $S + P = 1$.

3.7.4 Neuron Functions

During locomotion, a stick insect's leg is in one of two mutually exclusive phases: stance, where it supports the body on the ground and moves backward during forward walking. And swing, where the leg is lifted off the ground, and propelled in the walking direction [65]. In cats and locusts, it was found that some interneurons fire during swing, stance, or the transition between swing and stance [48, 49]. Since the movement primitive neurons combine information from all joints in the leg, it was hypothesized that some movement primitive neurons encode for swing, stance, or transitions between them.

In the dataset, the labeled leg-specific swing and stance phases were binned into 20 bins. Neuron spike events within these bins were tallied, and the likelihood of spiking during each bin was measured to construct a peri-stimulus time histogram (PSTH). This methodology proved useful for identifying phase encoding in specific primitive neurons.

To reveal general trends, a dimensionless number was assigned to each movement primitive neuron. the ratio between swing and stance spikes:

$$r_{\text{sw/st}} = \frac{N_{\text{swing}}}{N_{\text{stance}}}, \tag{37}$$

where N_{swing} and N_{stance} are the number of spikes that occur during the swing and stance phases, respectively. If $r_{\text{sw/st}} = 1$ or $r_{\text{sw/st}} = 0$, the movement primitive neuron exclusively fires during the swing or stance phase,

respectively. This ratio was calculated for each neuron, categorized by joint, leg, and input neuron type (e.g. vel_+ or $None$). For a broader analysis, primitive neurons with the same input neuron were grouped in a separate plot.

Figure 8: Stick insect body pitch over time, grey shading highlights intervals where body pitch angles exceed 10°, approximating climbing on a stair. Adapted from Gollin and Dürr [11]

3.8 Layer Four: Posture Layer

It was hypothesized that distributed proprioceptive information is processed to generate a three-dimensional representation of body posture in the stick insect [2, 11, 12]. In the proposed network, layer three introduced 672 unique primitive movement neurons, with 112 neurons dedicated to each of the six legs. Layer four aimed to utilize this information and estimate the insects' body pitch. in the work of Cohen, a simple regression model was used to generate a body pitch time course. To improve on this approach, the regression model was replaced by a spiking neuron layer: two neurons connected to movement primitive neurons of the preceding layer. The neurons spike during periods of high and low body pitch, respectively. The difference in the spike rate between these neurons served as the body pitch estimate. Additionally, a simpler model, the climbing classifier, was constructed. This was a singular neuron, that only fired during climbing.

3.8.1 Walking and Climbing Biases

During trials, the stick insect alternated between walking and climbing up steps. During walking, the body pitch exhibited slight fluctuations around zero (indicating the thorax parallel to the substrate). However, upon encountering a stair, the body pitch jumped to angles exceeding 10°, as illustrated in Figure 8. Consequently, a clear differentiation in body pitch between climbing and walking phases was observed. To leverage these phases, the neurons in the movement primitive layer (layer three) were investigated for their spiking bias during climbing and walking. Specifically, all spikes of the primitive neuron i were counted as a climbing spike (N_i^{climb}) if the body pitch exceeded 10° during a spike and as a walking spike (N_i^{walk}) if the body pitch remained below 10° during a spike. The ratio between climbing and walking spikes was defined as follows:

$$r_i = \frac{N_i^{\text{climb}}}{N_i^{\text{walk}}}. \tag{38}$$

If $r_i > 1$ or $r_i < 1$, the primitive neuron exhibited a bias for spiking during climbing or walking, respectively. The greater the deviation from 1, the more pronounced the bias.

3.8.2 Climbing Classifier Neuron

The climbing classifier neuron (CCN) was designed to spike when the body pitch exceeded 10°. To achieve this, the simplified LIF model applied in layer three proved adequate, with neuron and synaptic dynamics governed by Eqs. (33), (34), and (35). Primitive neurons exhibiting a significant climbing bias ($r_i > 2$) were connected to the CCN through excitatory synapses with weight ω_{exc}, whereas those biased toward walking ($r_i < \frac{1}{2}$) were connected through inhibitory synapses with weight ω_{inh}. Primitive neurons outside this range were not connected.

The body pitch time courses were segmented into 50 equally sized bins. For each bin, it was determined whether a spike occurred (predicted condition) and whether the body pitch exceeded 10° (actual condition). Subsequently, a confusion matrix was constructed following the methodology outlined in the last paragraph of Section 3.7.3. In the confusion matrix, climbing was designated as the positive condition and walking as the negative condition. The accuracy of the model was assessed using the MCC metric calculated using Eq. (36) while varying the strengths of the excitatory and inhibitory synapses. The r_i values were extracted from nine trials separate from the two trials used for optimization and estimation. With this approach, the model was "trained" on a dataset separate from testing.

3.8.3 Posture Neurons

The posture neurons' objective is to encode body pitch through spike rate over time. The architecture resembles that of the climbing classifier neuron described in Section 3.8.2. However, in this setup, two distinct neurons are employed. Climbing-biased primitive neurons are connected through excitatory synapses (ω_{up}) to one neuron, while walking-biased primitive neurons are connected through excitatory synapses to the other (ω_{down}). This arrangement results in two distinct spike rates, with one neuron exhibiting higher activity during climbing and the other during walking. Subtracting the walking neuron's spike rate from the climbing neuron's yields a combined spike rate resembling body pitch. This spiking pattern is expected to be noisy. By setting $\Delta T = 3\,\text{s}$ in Eq. (4), a running average can be plotted, smoothing out fluctuations. Subsequently, the firing rate and real body pitch are Z-normalized. They

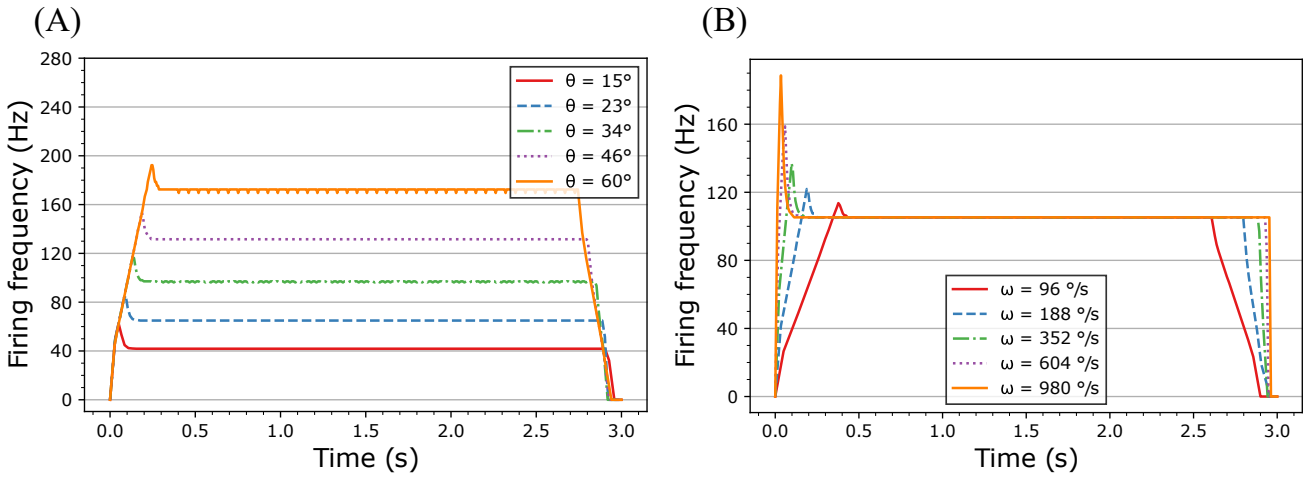

Figure 9: Firing frequency (Hz) as a function of time (s) for a sensory neuron stimulated by a ramp function. (A) The ramp function increases linearly at a constant velocity of $60.1\,^\circ\,\mathrm{s}^{-1}$ from 0° to varying end angles θ. (B) The ramp function increases linearly from 0° to 37° with varying angular velocities ω. Parameters were optimized to resemble the dynamics of axons from the lateral scapal hair plate in the American cockrach obtained by Okada and Toh (2001) [15].

are compared using the DTW method clarified in Section 3.5.3, providing an error estimate. To minimize error (DTW score), the bias ratio (r) for climbing neurons ($r_i > r$) and walking neurons ($r_i < \frac{1}{r}$) was varied within the range 1.3 to 3.5 with 6 equidistantly spaced steps. Additionally, the synaptic weights (ω_{up} and ω_{down}) were varied from 0 mV to 20 mV with 15 equidistantly spaced steps.

4 Results

This section highlights the results obtained using the methodology outlined in the preceding section. Similar to the methods Section, this Section examines the results layer by layer. Trials conducted on a flat substrate (without steps) were employed for layers one through three. If not stated otherwise, results are averaged for 78 trials. In the case of layer four, the trials involved two steps of 48 mm, with 12 functional trials. This section does not include detailed findings related to the effects of the model's parameters on neuron dynamics if already performed by Cohen. Interested readers are referred to Cohen's work (2020) [12] for further exploration of this aspect.

4.1 Layer One: Hair Field Layer

Table 1: Initial parameters for the AdEx model.

C	g_{l}	E_{L}	V_{T}	ΔT
200 pF	2 nS	−70 mV	−50 mV	2 mV

a	τ_ω	b	V_{R}
2 nS	50 ms	50-350 pA	58 mV

The initial AdEx parameters were adopted from Naud et al. (2008) [66] and subsequently adjusted by Cohen. Specifically, the leak conductance (g_{l}) was decreased from 12 nS to 2 nS. This modification resulted in a reduction of the rheobase current, which is the minimum current required to evoke an action potential. This allows the sensory neuron to fire at low input currents, and therefore at low hair deflections [12]. Additionally, the time constant τ_ω was lowered to 50 ms for quicker responses further down the network. the initial parameters for the AdEx model are given by Table 1.

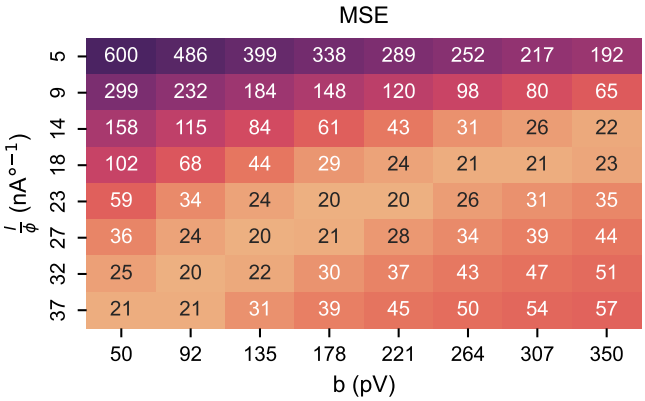

Figure 10: A heatmap depicting the error E, computed using Eq. (11), for a single sensory neuron. I/ϕ and b are varied from $5.0\,\mathrm{nA}\,^{\circ -1}$ to $37.0\,\mathrm{nA}\,^{\circ -1}$ and 50 pV to 350 pV, respectively.

A single tactile hair was subjected to stimulation using a ramp and hold function, following the procedure outlined in Section 3.4.3. The error E from Eq. (11) was computed at each iteration of a parameter sweep

involving I/ϕ and b. The corresponding results are illustrated in the heat map in Figure 10. A minimum error of 20 is observed for several results. The values $I/\phi = 18.0\,\mathrm{nA}\,^{\circ -1}$ and $b = 307\,\mathrm{pV}$ were randomly chosen from these results, these values will be adopted for the remainder of the thesis.

The time courses for both experiments are illustrated in Figure 9. The Figure depicts spiking dynamics over time for a sensory neuron that is stimulated by a ramp and hold function. The ramp function varies its end angle (A) or its angular velocity (B). Time courses can be compared directly to spiking dynamics outlined in Okada and Toh's study (2001) [15], illustrated in Figure 2. However, the angular velocities were quadrupeled and the total simulation time was divided by four as described in Section 3.4.3. It is clear from the Figures that the sensory neuron has similar general dynamics as the experimental values. During the ramp phase of the input, the firing frequency rapidly rises to a peak as the ramp transitions into a constant input. After the peak, the firing rate converges to a steady state. As the input ramps back to zero, the firing rate follows suit, linearly decreasing until it reaches zero. However, differences can be found in the details. there is considerable noise in the experimental data. In contrast, the simulated model is devoid of any noise, since none were introduced. Furthermore, the model reaches a steady state within a few seconds, whereas the experimental data displays a continuous decay throughout the entire duration of the experiment.

The firing frequency peaks at constant angular velocities (Figures 9A and 2A) are around 110 % of the steady-state conditions in the model. However, in the experimental data, these peaks are approximately 150 % of the steady-state firing rate. Moreover, in the experimental data, the low-end deflection angles (e.g. $\theta = 15°$) only produce a response during the onset of the ramp function, not during the steady state. This behavior is not observed in the simulated model, where low deflection angles do provoke a response in the neuron. Additionally, the steady-state frequencies in the simulation align closely with experimental results.

The dynamics for constant end angles (depicted in Figures 9B and 2B) display a higher degree of similarity. the steady-state spike rate of the model is inside the noise range of the experimental data. However, The peaks are slightly lower: 98 Hz - 150 Hz for the model compared to 118 Hz - 166 Hz for the experiment.

Table 2: Initial parameters for the position interneuron.

E_L	V_T	τ	τ_ω	τ_{epsp}
−70 mV	−50 mV	25 ms	3-18 ms	6 ms

b	V_{R}
1-16 mV	−70 mV

4.2 Layer Two: Position Layer

the parameters for the position interneuron were initially adopted from the research by Cohen, which are tabulated in Table 2. The synaptic parameters b and τ_ω will undergo optimization in section 4.2.2.

4.2.1 Binary Hair Field

With the sensory neuron optimized, 100 hairs were organized at each joint, forming two hair fields of 50 hairs each ($N_{\mathrm{h}}^{(1)} = N_{\mathrm{h}}^{(2)} = 50$). The joint angle range $\theta_{\mathrm{max}}^{(j)}$ and $\theta_{\mathrm{min}}^{(j)}$ are defined as the maxima and mimima of the joint angle time course. For the position interneurons, half of the hairs are connected, as was clarified in Section 3.5.1 and Figure 5. On the right axis, Figure 11A depicts a 10-second time course for the α joint (thorax-coxa) of the right anterior leg in black. The dotted line highlights the division between ventral and dorsal positions. The left axis shows a hair field raster plot, where each blue or red dot signifies a ventral or dorsal spike for tactile hair i, respectively. Due to the large number of spikes, the dots coalesce into a continuous line.

Figure 11A perfectly highlights the directional sensitivity of the hair field, with mirrored encoding observed in the ventral and dorsal domains. In the ventral domain, increasing joint angles prompt additional neurons to activate, whereas in the dorsal domain, reduced joint angles activate more neurons. If the joint was at rest, only the initial ventral and dorsal neurons fired, due to the predefined overlap. The tactile hair activity closely tracks the joint angle time course, demonstrating a near-perfect alignment.

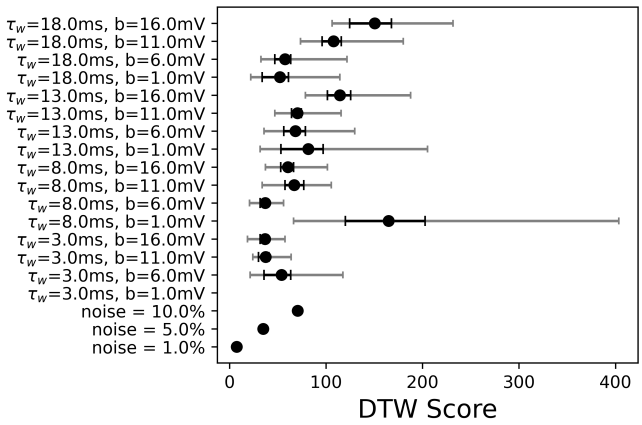

Figure 12: DTW scores for position interneurons displayed with median values (black dot), 50 % range (black whiskers), and maximum/minimum results (grey whiskers), for different parameters and three noise values.

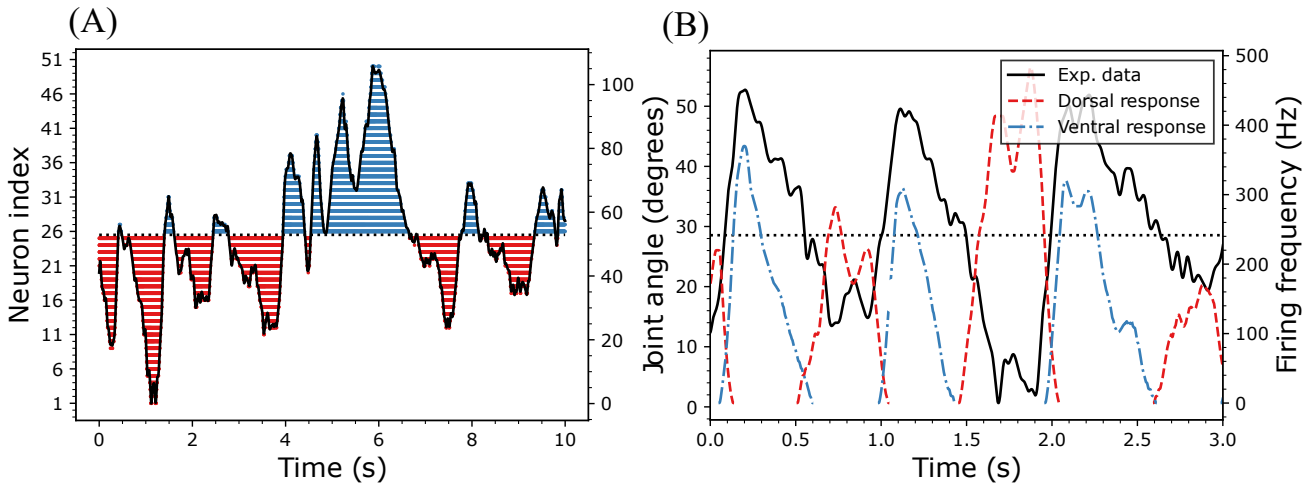

Figure 11: A 10-second time course for the α joint (thorax-coxa) of the right anterior leg is depicted in black. (A) The dotted line delineates the division between ventral and dorsal positions. The left axis displays a hair field raster plot, where each blue or red dot represents a ventral or dorsal spike for tactile hair i, respectively. The large number of spikes causes the dots to merge into a continuous line. (B) Firing frequency time course for the ventral and dorsal neurons.

4.2.2 Position Encoding Optimization

Figure 12 depicts the DTW score between the model prediction and ground truth averaged over 71 trials and 18 joint angles. The simulations with $\tau_\omega = 3\,\text{ms}$ and $b = 16\,\text{mV}$ yielded the best performance, achieving a DTW score slightly above 5 % Gaussian noise. These parameter values were used for the remaining portion of the thesis. Figure 11B illustrates a three-second joint angle time course and spike rates of ventral and dorsal neurons for the α joint (thorax-coxa) of the right anterior leg in black. The ventral neuron fired when the joint angle was larger than the rest angle (dotted line), while the dorsal neuron fired when the joint angle was lower. Spike rates fluctuated between 0 and 500 Hz and roughly followed the joint angle. However, finer details were lost.

4.3 Layer Two: Movement Layer

Table 3: Initial parameters for the adapted velocity interneuron.

τ_G	τ_l	τ_h^-	τ_h^+	τ_b
5 ms	1 ms	1 −3 ms	1 ms	1 ms

p	V_T	V_R	V_h	G_R
0.01	−50 mV	−70 mV	−53 mV	17 mV

Table 3 summarizes the parameter values for the adapted velocity interneuron. When the first presynaptic spike reached the synapse, the synaptic strength reached its maximum ($G_\text{R} = 17\,\text{mV}$), causing the voltage to increase from V_R to V_h. As the voltage matched the gating voltage, bursting initiated, leading to a reduction of G_R to 1 % of its initial strength ($p = 0.01$) due to strong self-inhibition. The modification of τ_h^- determined the number of spikes during a bursting event and will be optimized in the next section on spike rate control. τ_h^+ was set equal to the simulation time step, allowing quick initiation of a new bursting event after the end of the previous event. Setting τ_G to a low value allowed the synapse to transmit spikes after a short inactive period (e.g., rapid velocity changes) while ensuring sufficient time to suppress spikes during the same deflection event. The other time constant values were kept relatively low, minimizing inertia in the neuron. However, adjusting these parameter values had minimal impact on performance.

Table 4: Initial parameters for the novel velocity interneuron.

τ	V_T	V_R	ω
5 ms	−50 mV	−70 mV	10.5-11.5 mV

In contrast to the adapted velocity interneuron, the parameters of the novel velocity interneuron are straightforward (see Table 4). Similar to other neurons, the threshold and reset voltages adhere to their standard values. The cutoff frequency, denoted f_c, is a function of τ and ω. Setting the time constant to a low value ensured good accuracy. the optimal range for ω was 10.5-11.5 mV, determined through trial and error. This range will be employed in the subsequent section to investigate spike rate control.

4.3.1 Spike Rate Control

Figure 13 depicts the spike rate response of a velocity interneuron as a function of joint angle velocity for, (A)

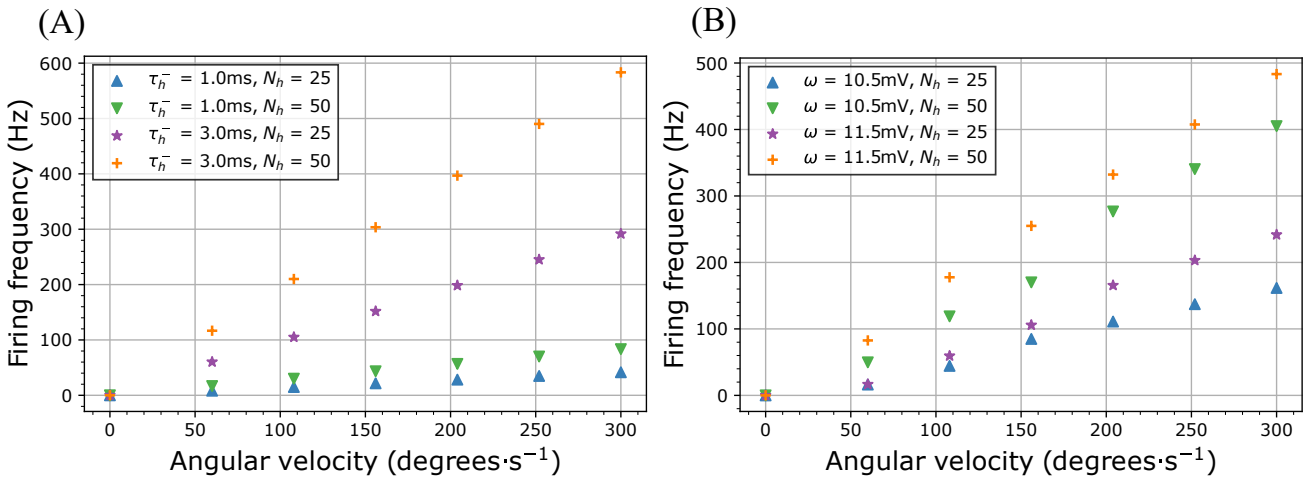

Figure 13: Firing frequency plotted against angular velocity for (A) the modified model and (B) the novel model. model parameters τ_- and ω and the number of hairs N_h are varied.

the modified model and, (B) the novel model. In both scenarios, doubling the number of hairs from 25 to 50 doubled the spike rate and firing frequency increased linearly with angular velocity for both models. However, the linearity of the novel model (B) was imperfect, particularly at small angular velocities. As anticipated, variables τ_h^- and ω contributed to the increase in spike rate. The IFB neuron allowed great variability in the spike rate, demonstrating an increase of approximately 750 % or more if required. In contrast, the novel model allowed a variability of around 200 %, but its initial spike rate ($\omega = 10.5\,\mathrm{mV}$) substantially exceeded the baseline of the modified model. The spike rate of the novel model cannot increase indefinitely. At a certain synaptic weight, the cutoff frequency matches the steady-state frequency and velocity encoding ceases. For both models, parameter values that yielded higher spike rates were adopted for the rest of the thesis, namely $\tau_\mathrm{h}^- = 3\,\mathrm{ms}$ and $\omega = 11.5\,\mathrm{mV}$.

Table 5: Confusion matrix and accuracy parameters for the adapted velocity interneuron

		Act. Positive	Act. Negative	Total
Pred.	Positive	684550	35541	720091
	Negative	34271	837439	871710
	Total	718821	872980	1591801

Accuracy	TPR	TNR
0.956	0.951	0.960

Table 6: Confusion matrix and accuracy parameters for the novel velocity interneuron

		Act. Positive	Act. Negative	Total
Pred.	Positive	581345	46339	627684
	Negative	47663	643021	690684
	Total	629008	689360	131368

Accuracy	TPR	TNR
0.929	0.924	0.933

4.3.2 Spiking Dynamics

Figures 14A and B depict individual spikes for forward and backward direction neurons in the adapted and novel model, respectively. In Figure 14A, the bursting nature of the IFB neuron is evident, with additional spikes occurring shortly after the initial one. However, these spikes tend to cluster together, resulting in alternating periods of spike clusters and no spikes. In contrast, Figure 14B shows that spikes are distributed uniformly for the novel model. However, at $t = 4\,\mathrm{s} - 4.5\,\mathrm{s}$, the model practically does not encode small changes in velocity, similarly to Figure 14B.

Tables 5 and 6 show the confusion matrix for the adapted and novel models, respectively. The confusion matrix was determined based on 79 trials, which involved 2 velocity interneurons at each of the 18 joints. From the confusion matrix, the accuracy, TPR and the TNR were computed using Eq. (30). The positives and negatives were balanced, confirming the suitibility of the simple accuracy score. TPR and TNR were relatively similar, indicating a balance between the firing rate of forward and backward neurons. Both models perform accurately. However, the modified model accuracy is 2.7 % higher than the novel model.

In Figure 14C and D, black traces illustrate a one-second time course of the velocity of the α joint (thorax-

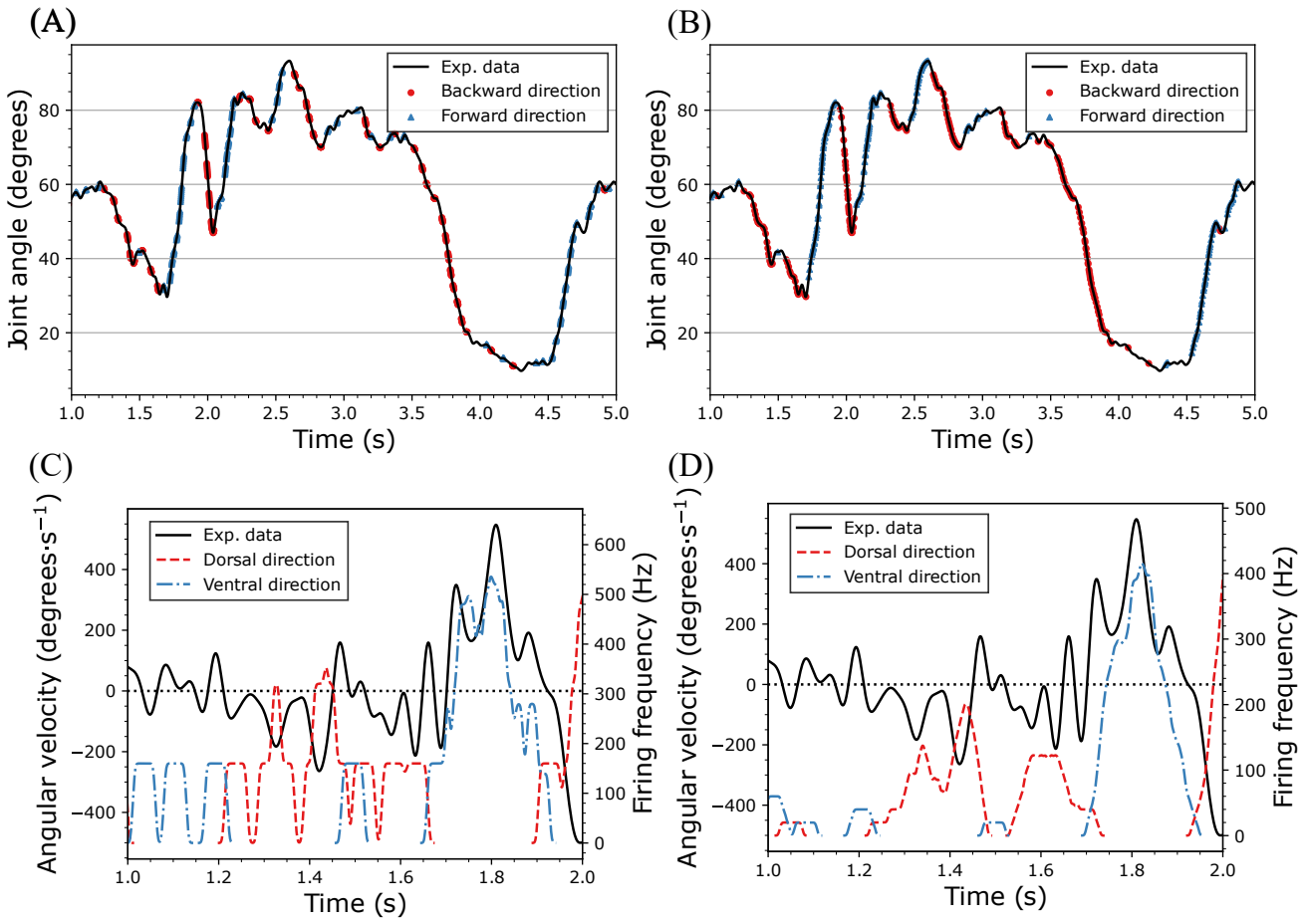

Figure 14: (A&B) Black traces represent a 4-second time course of the α joint (thorax-coxa) for the right anterior leg. Scatter plots overlay individual spikes on the joint angle time course for the modified model (A) and the novel model (B).1 secondBlack traces depict a 1-second time course of the α joint velocity (thorax-coxa) for the right anterior leg. Spike rates are plotted for the ventral and dorsal direction velocity interneurons in the modified model (C) and the novel model (D).

coxa) for the right anterior leg in addition to spike rates for the ventral and dorsal direction velocity interneurons. Both methods exhibit firing at appropriate times, such as the forward direction velocity interneuron firing when the velocity is positive. However, finer details are lost for both models. In particular, clustering of spikes for the modified model (Figure 14C) leads to a discretized spike rate and a loss of sensitivity to small changes in velocities.

4.4 Layer Three: Movement Primitive Layer

Table 7: Initial parameters for the movement primitive neurons.

τ	V_T	V_R	ω_{pos} & ω_{vel}
0.5-3.5 ms	−50 mV	−70 mV	3-18 mV

Table 7 features the parameters for the movement primitive layer. While the threshold and reset voltages adhere to standard values, the parameters τ, ω_{pos}, and ω_{vel} considerably influenced model performance and underwent optimization.

4.4.1 Optimization

Figure 15A shows the MCC versus the τ for seven subsets of movement primitive neurons, detailed in Section 3.7.1. The synaptic weights of position (ω_{pos}) and velocity interneurons (ω_{vel}) were individually adjusted (using the grid method) from 3 mV to 18 mV, with increments of 1.5 mV. The Figure highlights inconsistent performance across subsets, with those featuring more position interneurons generally outperforming those with velocity interneurons. Furthermore, subsets with three inputs had improved performance compared to those with only two inputs. The mean MCC peaked at 0.56.

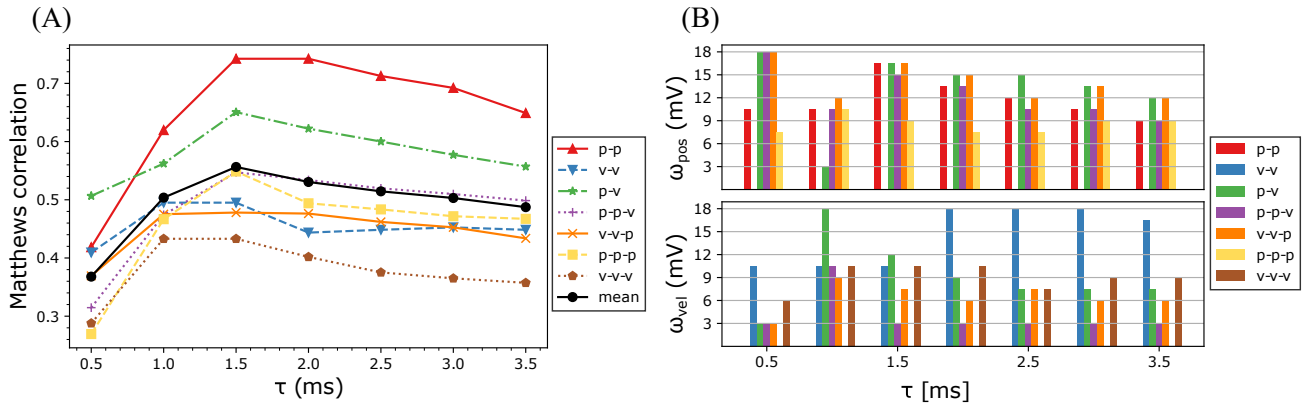

Figure 15: A. MCC as a function of the time constant τ, considering seven subsets detailed in Section 3.7.1, along with the mean for optimal synaptic weight values. B. optimal weights ω_{pos} and ω_{vel} for several values of the time constant τ for the same seven subsets

Table 8: Optimal weights for the movement primitive neurons, extracted from Figure 15B.

	p-p	v-v	p-v	p-p-v	v-v-p
ω_{pos} (mV)	16.5	-	16.5	15.0	16.5
ω_{vel} (mV)	-	10.5	12.0	3.0	7.5

	p-p-p	v-v-v
ω_{pos} (mV)	9.0	-
ω_{vel} (mV)	-	10.5

Figure 15B highlights the weights corresponding to the optimal MCC value for each subset at each time constant. Generally, the optimal ω_{pos} is higher than ω_{vel}, and both decrease as the time constant increases for time constants higher than the timestep $dt = 1\,\text{ms}$. Some exceptions include the high ω_{vel} value for the $v-v$ subset at high time constants and $p-v$ at $\tau = 1\,\text{ms}$. Table 8 lists the optimal weights for the movement primitive neuron at the best mean MCC value for the optimal time constant ($\tau = 1.5\,\text{ms}$).

4.4.2 Swing and Stance Encoding

Figure 16A illustrates the swing-to-stance spikes ratio ($r_{\text{sw/st}}$) for all 672 movement primitive neurons, with color coding for extracting the specific neurons associated with swing or stance phases. As an example, in the anterior right leg, the (vel_+, *None*, vel_+) primitive neuron strongly encodes swing, while the (pos_+, pos_+, pos_-) primitive neuron strongly encodes stance. Figure 17A and B depict the likelihood of spiking during swing and stance bins for these primitive movement neurons, respectively. Swing encoding (Figure 17A) is strongest in the middle of the swing phase, while the stance encoding (Figure 17B) also peaks, albeit with an irregular structure. There are countless examples of regular and irregular swing and stance encoding for other movement primitive neurons.

Figure 16B combines data points of Figure 16A for the input parameters (vel_+, pos_+, etc.), *None* is omitted. Combining data points allows for easier comparison between joints, legs and input parameters. As an additional aid, Tables 9 and 10 tabulate the scores of a paired t-test between vel_--vel_+ and pos_--pos_+, respectively. The critical values for a two-sided test with a sample size n of 24 are provided for significance levels of 0.1 % (red), 1 % (blue), and 5 % (green) as 3.792 ($p < 0.001$), 2.819 ($p < 0.01$), and 2.074 ($p < 0.05$), respectively. These critical values serve as thresholds for hypothesis testing, with the associated p-values indicating the level of statistical significance. A test statistic exceeding the critical value leads to the rejection of the null hypothesis, and smaller p-values suggest stronger evidence against the null hypothesis [67].

Strong encoding (red, $p < 0.001$) for swing and stance is symmetric for both sides of the body. Regarding the velocity input parameter (Table 9), the α joint serves as a robust indicator for all legs, consistently encoding for forward movement during the swing phase. For the β joint, backward movement weakly encodes the swing phase in the front legs, no encoding is observed in the middle leg, and strong encoding occurs in the hind leg during forward movement. The γ joint, on the other hand, displays good encoding indicators in both the front and hind legs, with reversed directions. For the position input parameter (Table 10), weak encoding (blue, green, black, $p > 0.001$) is not symmetrical on both sides, but strong encoding remains symmetrical. Whenever encoding is present, the swing phase is consistently encoded by the ventral position interneuron. Specifically, the γ joint strongly encodes for swing with the ventral position, the β joint shows encoding exclusively in the middle and hind legs, while the α joint exhibits only weak, or no encoding.

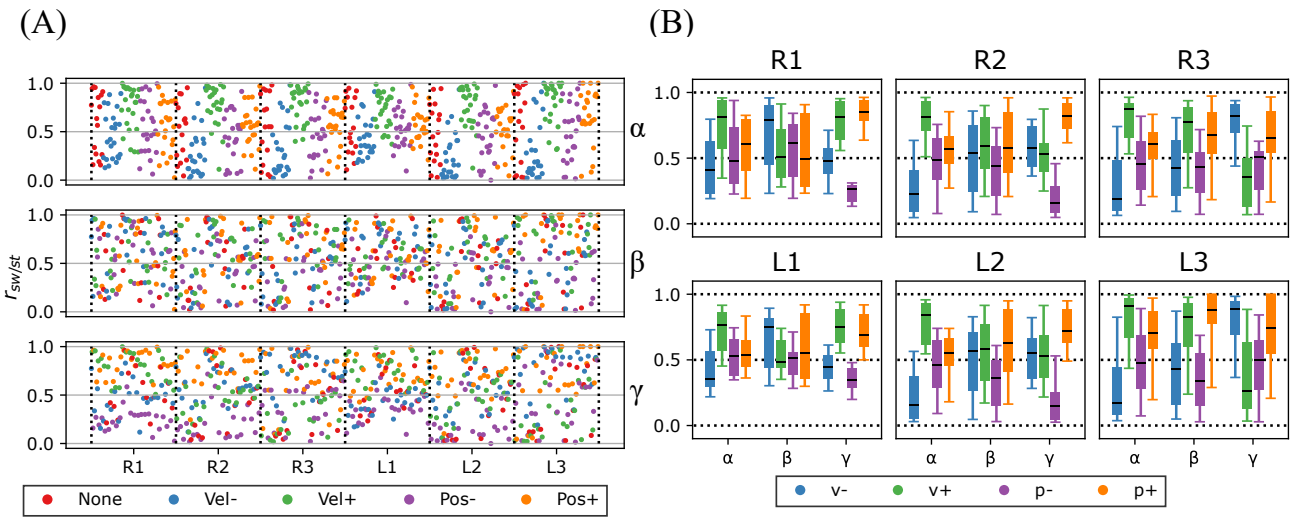

Figure 16: A. Ratio of spikes during swing and during stance for all 672 movement primitive neurons, divided by joint and leg (three joints and six legs). B. The datapoints from A grouped into velocity and position interneurons for the three joints and six legs. The black line represents the median value, the box encompasses the first 50 percent, and within the whiskers are the first 90 percent

Table 9: paired t-test scores between vel_- and vel_+ for six legs and three joints. $p < 0.001$, $p < 0.01$, and $p < 0.05$ are denoted as red, blue and green, respectively.

	R1	R2	R3	L1	L2	L3
α	-7.53	-8.76	-7.94	-7.53	-9.22	-7.56
β	3.68	-1.61	-4.58	3.07	-1.23	-4.20
γ	-7.14	1.97	6.93	-7.84	-0.33	6.33

Table 10: paired t-test scores between pos_- and pos_+ for six legs and three joints. $p < 0.001$, $p < 0.01$, and $p < 0.05$ are denoted as red, blue and green, respectively.

	R1	R2	R3	L1	L2	L3
α	-0.54	-2.72	-2.13	-1.97	-1.03	-3.50
β	0.34	-7.47	-5.35	-2.87	-5.15	-7.97
γ	-19.75	-17.04	-5.25	-9.60	-11.73	-4.66

Movement primitive neurons also encode other phases than purely swing and stance. Figure 17C is a PSTH plot for the (vel_-, vel_-, pos_-) movement primitive neuron for the left middle leg. The neuron encodes the transition from swing to stance and stance to swing. Figure 17D shows the (vel_+, $None$, pos_+) primitive interneuron of the left posterior leg. This neuron has strong beginning of swing encoding and a weak end of stance encoding.

4.5 Layer Four: Posture Layer

In this section, the network is tasked to estimate climbing and body pitch. To facilitate this, significant changes in body pitch are necessary. Therefore, the network receives information of 11 unrestrained climbing trials with steps of 48 mm.

Table 11: Initial parameters for the climbing classifier (top) and body pitch estimation neurons (bottom).

τ	V_T	V_R	ω_{inh}	ω_{exc}
50 ms	−50 mV	−70 mV	0-0.2 mV	0-0.13 mV

τ	V_T	V_R	ω_{up}	ω_{down}
50 ms	−50 mV	−70 mV	0-20 mV	0-20 mV

Table 11 outlines the parameters of the climbing classifier neuron and body pitch estimation neurons. The time constants, threshold voltages, and reset voltages were held constant. For the climbing classifier, the excitatory (ω_{exc}) and inhibitory weights (ω_{inh}) were varied to optimize performance. For the body pitch estimator, ω_{up} and ω_{down} were varied.

4.6 Climbing Classifier

In this work, climbing is defined as the metathorax inclination of more than 10° relative to the experimental substrate. The climbing classifier is tasked to fire whenever the insect is climbing. Figure 18A shows the MCC of the climbing classifier while varying the excitatory weight ω_{exc} from 0.05 mV to 0.13 mV and the inhibitory weight ω_{inh} from 0.0 mV to 0.2 mV. The neuron is most accurate (MCC = 0.59) for $\omega_{exc} = 0.085$ mV and $\omega_{inh} = 0.04$ mV. Figure 18B illustrates the activity of the climbing classifier for a single climbing trial. The climbing classifier mainly spikes during climbing, especially at higher body pitch angles. At angles closer to 10°, the spike rate is significantly lower. There are six

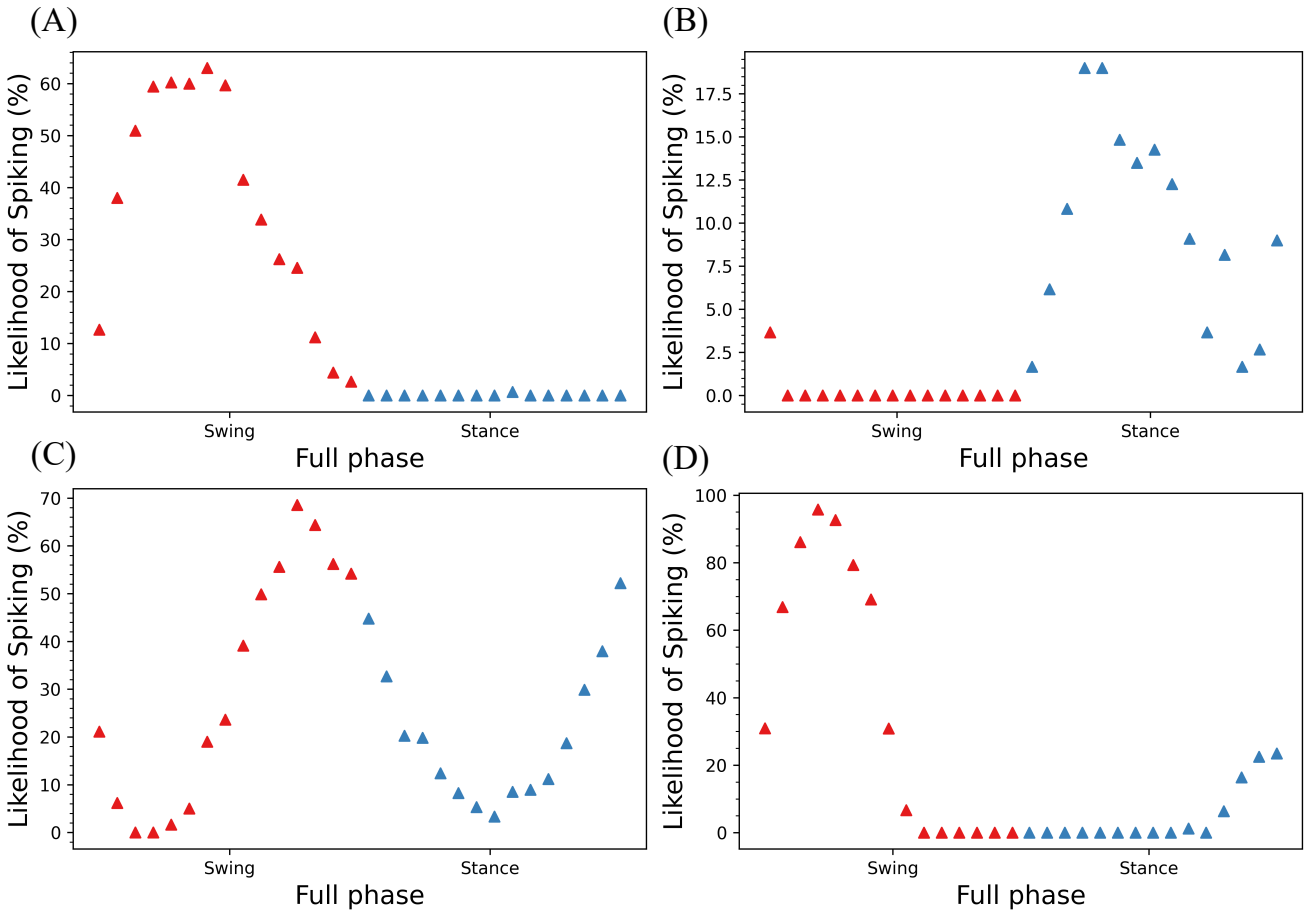

Figure 17: Likelihood of a neuron to spike in the swing or stance phase. The swing and stance phases are binned in 20 bins each. A. Right anterior leg, (vel_+, $None$, vel_+) primitive interneuron, swing encoding. B. Right anterior leg, (pos_+, pos_+, pos_-) primitive interneuron, stance encoding. C. left middle leg, (vel_-, vel_-, pos_-) primitive interneuron, transition encoding. D. left posterior leg, (vel_+, $None$, pos_+) primitive interneuron, strong beginning of swing and weak end of stance encoding.

spikes at body pitch angles below 10°. Table 12 indicates the participation of neurons in climbing (N_n) per leg. The data reveals that the front and middle legs contribute more compared to the hind legs. Moreover, there is nearly equal participation on the left and right sides of the body.

Table 12: The number of neurons that contribute to the climbing classifier (N_n), per leg.

Leg	R1	R2	R3	L1	L2	L3
N_n	52	52	35	50	54	32

4.7 Posture Estimation

The posture neuron was designed to generate a time course of body pitch. In Figure 18C, the DTW score for body pitch estimation is plotted against the ground truth while varying ω (both ω_down and ω_up) and $r_\mathrm{sw/st}$. For most values of $r_\mathrm{sw/st}$, the optimal synaptic strength was slightly above or just below 10 mV. Beyond 10 mV, increasing the synaptic weight did not impact the model's accuracy. The selection of the appropriate $r_\mathrm{sw/st}$ value was crucial for achieving optimal accuracy. The best-performing parameter set was $\omega = 7.2$ mV and $r_{sw/st} = 3.06$, yielding a DTW score of 51, equivalent to the ground truth with and added Gaussian noise of 28.5 %.

Figure 18D displays the body pitch ground truth, model estimation ($\Delta T = 0.2$ s), and a moving average ($\Delta T = 3$ s) over time. Two trials are concatenated, each consisting of two steps. The model response captures significant swings in body pitch accurately but is affected by noise. The moving average mitigates the noise. Although the moving average aligns with major body pitch swings at the correct times, it doesn't include exact peak timings and finer details.

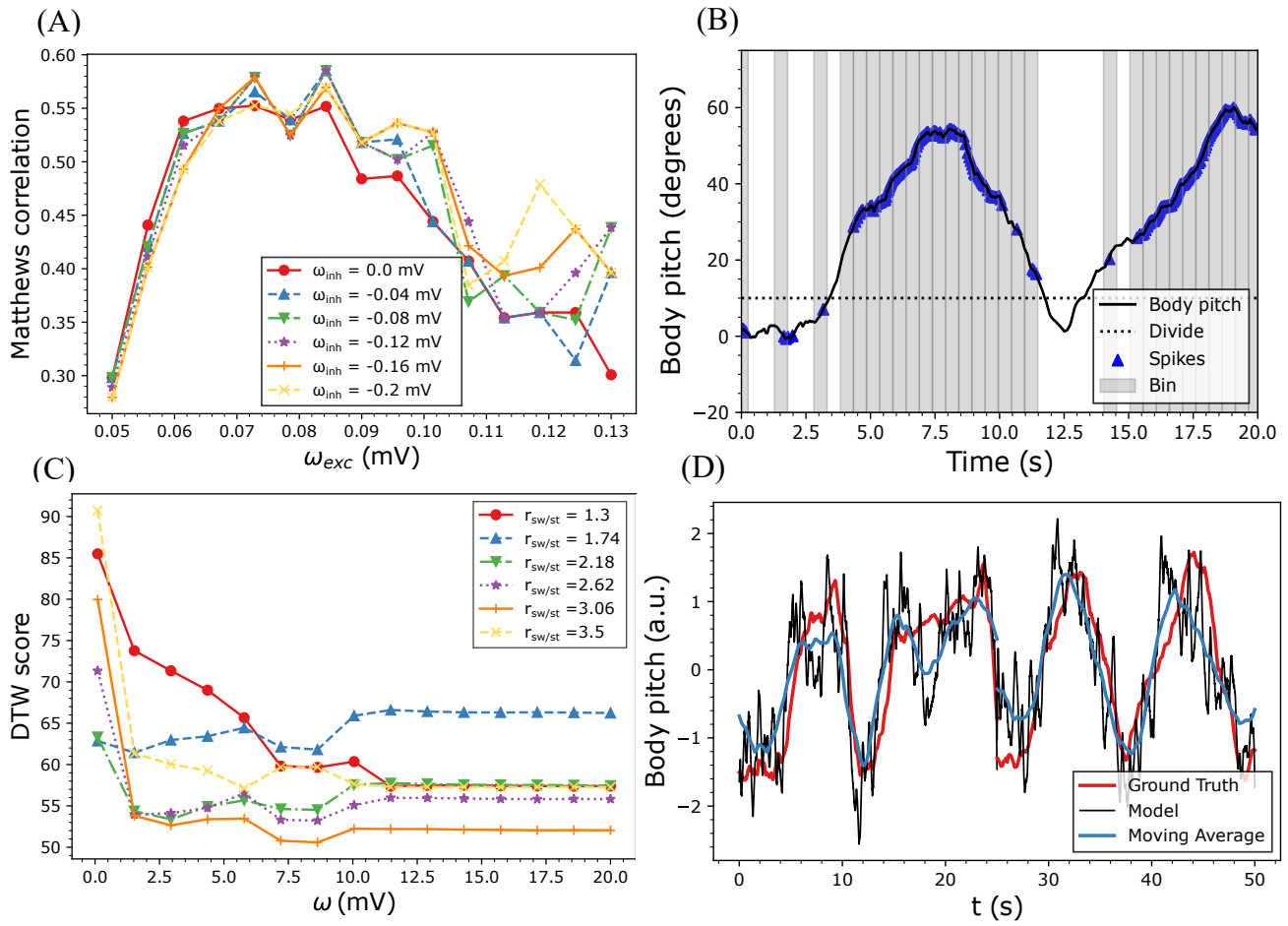

Figure 18: A. MCC of the climbing classifier while varying ω_{exc} and ω_{inh} B. Time-dependent plot of body pitch, with climbing classifier spikes superimposed using $\omega_{\text{exc}} = 0.085\,\text{mV}$ and $\omega_{\text{inh}} = 0.04\,\text{mV}$. A bin is flagged if at least one spike occurs within the bin. C. MCC of the body pitch neurons with varying ω (ω_{up} and ω_{down}) and $r_{\text{sw/st}}$. A DTW score of 51 corresponds to the ground truth with 28.5 % Gaussian noise. D. Body pitch ground truth, model prediction, and moving average over time. Two trials are concatenated, plotted for optimal values obtained in C ($r_{\text{sw/st}} = 3.06$ and $\omega = 7.2\,\text{mV}$).

5 Discussion

5.1 Layer One: Hair Field Layer

The hair field layer was designed to replicate the spiking dynamics of the axons in the lateral scapal hair plate of the American cockroach (Figure 2) [15] using an AdEx model (Figure 9). The adaptation term in the AdEx model allowed for a combined phasic and tonic response, and therefore copied the essential features of the observed experimental spike dynamics. Despite challenges such as the absence of inherent neuronal noise, spike rate mismatch, low angle encoding, and differing adaptation strengths, these dynamics provided a solid foundation for the rest of the network. The phasic and tonic responses in the sensory model were exploited by the velocity and position interneurons, respectively. In fact, intentionally shortening the time scale of the dynamics resulted in a reduced DTW score for the position interneuron, improving from 10 % Gaussian noise in Cohen's results to 5 % Gaussian noise in the results of the current work.

At the time scales suggested by the experimental results, τ_ω had to be in the range of 500 ms. This led to adaptation long after the direction of the joint angle changed, resulting in unnecessary delays in subsequent layers. However, slow adaptation is required to produce prolonged phasic behavior (as observed in the broad peak in Figures 2A and B). To address this, reducing the timescales allowed for phasic behavior while reducing τ_ω, thus improving performance in subsequent layers. The author believes that exercising this creative freedom is warranted since the dynamics were not derived from a stick insect, and specific spike rates are known to vary between species, individual insects or even different hair plates in the body [15]. Additionally, the main features of the dynamics were conserved.

Previous research has addressed the issue of model-

ing sensilla responses using abstract computational approaches, such as a Poisson spike generator [10, 11]. However, this method does not take into account the non-linear transform function that occurs between the the stimulus (i.e., deflection of the hair) and the response of the neuron. In contrast, the AdEx model applied in this study takes a raw input of joint angles without any pre-processing through high-pass and low-pass filters. The only pre-processing involved was converting the angles into deflection angles and then converting those angles into input current.

The model design was based on Cohen's work, with minor adjustments such as reducing the time scale and optimizing the hair row structure. A major change was transitioning from 40 hairs to 100 hairs (50 per hair row), this increased sensitivity significantly. While increasing the number of hairs indefinitely could further increase sensitivity, a biologically realistic amount of 50 hairs per hair row was chosen [34]. The current work also includes assumptions that Cohen made when designing the hair plate. These assumptions were made to simplify the problem. For example, it was assumed that tactile hairs were the same length, although there is evidence of variations in length [34, 68]. Another assumption was that the hair angle increased linearly with the joint angle. However, the morphology of the sensilla implies that linearity is correct [34]. The final assumption was that the hairs were arranged in an orderly manner in their receptive fields and slightly overlapped each other. However, research suggests that tactile hairs are actually arranged at regular intervals [17, 35, 36], lending some truth to this assumption. For further investigation, these assumptions could be overcome by accounting for differences in hair length, examining nonlinearities in hair angle, or optimizing hair distribution. As Cohen clarified in his work, an interesting approach would be the efficient coding hypothesis [69]. The hypothesis assumes that sensory systems are structured to efficiently represent the dynamic sensory stimuli that the animal encounters in its environment. Consequently, these systems are likely not organized in a perfectly linear structure, but rather are arranged to maximize coding for the most common stimulus sets encountered by the animal. This idea can also be extended to the structure of hair field rows, suggesting that hairs may have different receptive fields based on the probability distribution of joint positions.

5.2 Layer Two: Position Layer

The position layer was designed to integrate information from the hair field layer to encode joint position. This design draws inspiration from biological examples of position-encoding DINs [44, 7, 10], particularly the segregation of position interneurons into dorsal and ventral activated neurons [45, 7]. In alignment with the findings of Ache and Dürr (2015) [10], it is established that employing two hair fields (ventral and dorsal) is adequate for accurately estimating joint position in the presence of a natural stimulus.

In Figure 12, there is no DTW score available for the parameters $\tau_W = 3.0\,\text{mV}$ and $b = 1.0\,\text{mV}$. These synaptic parameters prove too low to facilitate postsynaptic spikes. Consequently, no DTW score is measurable. In scenarios with (too) high synaptic weights, firing frequency reaches the limit (1000 Hz) imposed by the timestep ($dt = 0.1\,\text{ms}$), resulting in the loss of finer details. This loss of detail contributes to an increased DTW score. The optimal parameter configuration leads to an improved precision of position estimation, reducing Gaussian noise from 10 % (as observed in Cohen's work) to slightly over 5 % (see Figure 12). Since the optimization for the position interneuron remained consistent, this improvement in accuracy can be attributed to the acceleration of tactile hair temporal dynamics in the preceding layer. Tactile hair dynamics were manually changed to the dynamics observed by Cohen, and performance was reduced to 10 % Gaussian noise, validating the previous claim. The remaining disparity between the actual joint angle and neuron estimation is largely ascribed to the inherent smoothness of the estimated time course (Figure 11B). The methodology for calculating firing frequency (Eq. 3) tends to smooth out finer details, and there may be further enhancements possible by reducing the simulation timestep. Ultimately, the estimation proved to be accurate enough for subsequent layers. Therefore, employing a simple LIF as the position interneuron is suitable.

5.3 Layer Two: Movement Layer

The velocity interneurons in the movement layer were designed to spike whenever the joint angle changed. Inspiration was drawn from evidence for a ON-type velocity sensitive encoding DINs in the stick insect antenna [7, 10, 70]. There is also evidence for velocity encoding DINs in the crickets' antenna [44] and the fruitfly [45]. However, the ON-type DINs found in the antenna were not directionally sensitive. Ache and Dürr (2015) [10] investigated three possible neuronal circuits that would achieve non-directionality: a post-inhibitory rebound system, an elaborate subsystem of excitatory and inhibitory DINs between the hair field and ON-type neuron, or another set of afferents with opposite directional sensitivity and only phasic components innervating the ON-type neuron. The first two options were deemed unlikely because post-inhibitory mechanisms were not observed in the neuron's spiking behavior and because of the short latency (∼11 ms) between the layers [12]. Therefore, the last possibility was partly incorporated into the architecture of the network. However, there is no direct evidence that the current implementation is biologically accurate. Firstly, the ventral and dorsal hair fields had to be extended to account for the sensitivity

range of the velocity interneurons. And as clarified earlier, the ON-type neuron was not direction sensitive like the proposed velocity interneurons [10]. Lastly, The current thesis only uses hair plate information to feed into the DINs. In insects, information from the chordotonal organ contributes velocity information to the proprioceptive system [30, 29, 24]. However, the current work shows that the phasic-tonic behaviour of the tactile hair can be exploited to extract both position and velocity information.

During the research phase, it was apparant that the spike rates of the velocity interneuron in Cohen's work was inherently tied to the number of tactile hairs. Additionally, the spike rate was found to be extremely low, 40 Hz at a joint velocity of $190\,^\circ\,s^{-1}$. To get sufficient overlap possibility in the subsequent (movement primitive) layer, these spike rates had to be significantly increased. To achieve sufficient spike rates, the number of tactile hairs had to be increased tenfold. However, the number of hairs would be biologically inaccurate. Therefore, the spike rate had to be increased independently from the number of hairs. Two models were proposed, the first added a bursting current (modified model) and the second exploited the phasic properties of the tactile hair (novel model). The modified model was slightly more accurate than the novel model, but both were more accurate than Cohen's model. The accuracy was improved from 0.904 to 0.956 for the modified model and 0.929 for the novel model. Additionally, both models allowed for a substantial increase in the spike rate, 400 Hz for the modified model, 340 Hz for the novel model relative to 40 Hz for Cohen's model at $203\,^\circ\,s^{-1}$. Since the number of hairs was multiplied by 2.5, both models inherently increased the spike rate by 3-4 times. The modified model could increase the spike rate even more by increasing τ_h^-, at the risk of more spikes occurring at the wrong time. The novel neuron spike rate could be improved further by increasing the phasic peak of the sensory neuron (Figure 9), but ω can not be increased to improve the spike rate. In case of the modified neuron, additional spikes occur after the initial spike independent from the joint direction. Therefore, each spike that is added has a chance of occurring after the velocity has changed direction, spiking at the wrong time. Moreover, clustering of spikes (Figure 14A) yields a staircase effect in the spike rate (Figure 14B), removing sensitivity to detail. To achieve a bursting event, several time constants had to be set incredibly low (equal to the timestep). And according to the literature: $\tau_h^+ >> \tau_h^-$, which is not true for the current model [58]. Even though accuracy and spike rates are slightly higher for the modified model, the novel model was chosen as superior due to the aforementioned reasons. Additionally, The novel model is extremely simple compared to the modified model, and the spikes are uniformly distributed. And phasic neurons encode velocity [28], just like the novel model, making it more biologically accurate. However, At slow joint movements, the phasic response of the sensory neuron decreases (Figure 9B), and the novel model will not fire. This effect is observed in Figure 14B, and is a limitation of the model.

The author believes that the existing movement layer is optimal given the current number of tactile hairs in the hair plate. Increasing the number of hairs could enhance sensitivity, and therefore accuracy. This would allow the interneuron to sense smaller changes in velocity. Another approach is adding a dedicated velocity-sensing mechanoreceptor (e.g. chordotonal organ), which could greatly increase sensitivity and accuracy if done correctly.

5.4 Layer Three: Movement Primitive Layer

Based on the hypothesis that motor movements consist of elementary units of motor reflexes known as "movement primitives" [71], the movement primitive neuron was devised to gather information from two or three of the joints and convey the spatio-temporal state of the entire leg. Movement primitives find their application in humanoid robots [72], and have been studied for executing motor behavior in both invertebrates and vertebrates across behavioral, muscular, and neural levels. Research into human reaching movements has revealed their organization into distinct movement blocks, each exhibiting similar spatio-temporal characteristics [71]. Inspired by the concept of movement primitives, Cohen postulated the existence of a corresponding sensory circuit closely interacting with motor primitive neurons. In this thesis, the movement primitive layer acts as this sensory circuit.

The movement primitive layer in Cohen's work had a high TPR but also a comparatively high false positive rate (FPR) [12]. Consequently, Cohen suggested that the movement primitives functioned as sub-optimal classifiers. Cohen proposes that either a more refined tuning scheme or an alternative neural/synaptic model may be necessary. The current author agrees with the former proposition. Throughout the research, it became evident that the inadequate performance of the movement primitive layer primarily stems from low spike rates in the preceding layers, poor optimization of synaptic/neural parameters within the movement primitive layer itself, and suboptimal accuracy of the preceding layers, in descending order of significance. Enhancements in accuracy and spike rate were investigated in preceding sections. Merging these accuracy improvements with synaptic and neuron optimization (see Figure 15) led to enhanced results for primitive neuron accuracy. Nevertheless, certain subsets outperformed others (see Figure 15A). Subsets that received information from position interneurons achieved enhanced accuracy in contrast to those incorporating velocity interneurons. This discrepancy can be attributed to better accuracy

and a higher spike frequency of the position interneuron. Position interneurons sustain constant spiking for extended periods when joint angles are high, whereas velocity interneurons exhibit shorter spike peaks. Despite similar spike peak rates, position interneurons therefore yield a higher total spike count. This hypothesis was tested by substantially increasing the number of hairs. This change significantly improved the accuracy of movement primitive neurons that received information from velocity interneurons, while those receiving information from position interneurons showed no significant improvement. Furthermore, position interneurons maintain sensitivity across the entire receptive field of a tactile hair, unlike velocity interneurons whose sensitivity is closely linked to the number of hairs in a hair plate, only firing during the onset of a complete hair deflection. Generally, subsets with two inputs outperformed those with three inputs. This discrepancy arises from the fact that three inputs require overlapping, which is less probable than with two inputs, consequently reducing the MCC.

A significant fraction of movement primitive neurons show swing or stance encoding. Firing predominantly during either the swing or stance phase (Figure 17A and B), similar to interneurons observed in locusts or cats [57, 49]. These neurons are used as an internal representation of swing and stance phases for each leg, which is a critical parameter of insect locomotion [73, 74]. Moreover, the proposed method allows for finer encoding, such as the beginning of the swing phase (Figure 17D). Another significant application is the requirement of phase information from other legs for swing/stance initiating motor neurons, particularly evident during phase transitions, which are pivotal for leg coordination [5, 6]. As an example, Figure 17C depicts a neuron that spikes during each phase transition.

The encoding of swing/stance phases is facilitated by interneurons supplying information to the movement primitive neurons. Analysis of Figure 16B and Tables 9 and 10 reveals that the α joint (protraction-retraction) strongly encodes for swing during forward movement, a finding corroborated by existing literature [6, 26]. This observation aligns with the biomechanics of leg movement, as during the swing phase, the entire leg moves forward while the α joint transitions from retraction to protraction. Therefore, during swing the α joint moves from ventral to dorsal position, leading to negligible swing or stance encoding by the α position interneuron. Additionally, the results suggest that the β joint (levation-depression) assumes a ventral position during the swing phase, reflecting the need for leg elevation during this phase. This effect is particularly pronounced in the middle and hind legs compared to the front legs. This could be explained by searching behavior in the front legs, keeping the tarsus close to the substrate [75]. Another significant indicator is the position of the γ joint (flexion-extension), which assumes a ventral position during the swing phase, indicating the forward extension of the tibia in preparation for a touchdown, increasing reach and elevating the tarsus from the substrate. Conversely, during stance, the tibia is pointed down, since the tarsus has to be planted firmly in the substrate for maximum grip. According to Tables 9 and 10, this pattern holds for all legs but is less pronounced in the hind legs. Moreover, the γ joint angle increases during swing in the front legs while decreasing in the hind legs, with no specific encoding observed in the middle legs. This effect is similar but inverted for the β joint.

5.5 Layer Four: Posture Layer

The posture layer was designed to serve two primary functions: one, to host an interneuron that spikes during climbing, and another to estimate body pitch. This layer received input from the movement primitive neurons of all six legs. The current work improves on Cohen's work by constructing the layer with spiking neurons rather than a deep neural network.

The performance of the climbing classifier is reduced significantly by just a few occasional spikes that fire at the wrong time (Figure 18B). This is a consequence of how the bins were counted. The MCC of 0.59 was therefore lower than realistic. During periods of high body pitch, the number of spikes increased rapidly, potentially making the climbing classifier a reliable indicator for climbing in the stick insect. However, a similar result could be obtained from attaching a high pass filter to the body pitch estimator neuron. Table 12 shows that the the front and middle legs contribute more to the climbing classifier, contrary to the findings of Gollin and Dürr (2018) [11], where the middle and hind legs were reported to have the greatest influence on body pitch. This result does confirm the suspicions raised by Cohen regarding the front legs in the discussion section of his thesis: *"It would be interesting to identify the contribution weight of different legs. The front legs might be thought to propagate more important information, since they are the first to be used during the climbing behavior."*

The body pitch estimator exhibited an error equivalent to the original body pitch when subjected to 28 % Gaussian noise. This corroborates findings from previous studies, suggesting the feasibility of estimating body pitch from proprioceptive information [11, 12]. Moreover, it adds the premise that body pitch estimation is achievable using only spiking neurons, thereby further reinforcing the idea that neural circuits in the stick insect can represent body pitch without a dedicated organ. The remarkable accuracy of this result is noteworthy given that the proprioceptive information passed through three spiking layers, compounding errors along the way. Additionally, the simplicity of constructing the neuron by observing spike behavior from the pre-

ceding layer and selecting for spike biases underscores the potential efficiency of such a method. However, despite these advancements, the error remains significant and can be attributed to the aforementioned factors. Furthermore, in a real stick insect, additional information is gathered from the campaniform sensilla, chordotonal organs, or possibly from other sources besides the joints. This supplementary information may be essential, as even with a DNN, previous research has failed to achieve perfect body pitch estimation solely using tactile hair proprioceptors [11, 12].

5.6 Future Scope

The present thesis represents an enhancement and expansion of the SNN initially proposed by Cohen. These enhancements stem from suggestions by Cohen, further research, and trial and error. However, there remain several areas where further enhancements are possible. Firstly, noise is an inherent aspect of all biological neuronal systems. It is present in every level of the CNS, from sensory to motor levels. Noise could come from external vibrations in the tactile hairs or stochastic intrinsic electrical fluctuations within the neural network [76]. Introducing noise into the system could enhance the claim of biological plausibility of the computational model. Another point is the sensitivity of the tactile hairs. The current author believes that the network performance is compromised by the velocity interneurons due to their limited sensitivity. As these interneurons respond solely during transitions from one receptive field to the next, their sensitivity is inherently linked to the number of hairs in the hair plate. Due to the biologically imposed constraint on the number of tactile hairs, sensitivity is limited. Therefore, including models of other types of proprioceptors (e.g. the chordotonal organ) may potentially improve velocity estimation. While the current thesis suggests that the phasic response of tactile hair can be utilized for velocity estimation, other more specialized proprioceptors might be more appropriate.

There is also potential for expansion of the proposed SNN. For instance, the dataset could be modified to incorporate kinematics data encompassing whole-body turning. This adjustment would enable the application of movement-primitive neurons to encode natural turning, encompassing yaw, and pitch rotations as the animal maneuvers around a pole. Another extension could involve spatial transfer of limb information. Dürr and Schilling (2018) [77] introduced the idea of an affordance space: "which is that part of peripersonal space within which contact-induced spatial estimates lie within the action ranges of more than one limb. Because the action volumes of limbs overlap in this affordance space, spatial information from one limb can be used to control the movement of another limb. Thus, it gives rise to an affordance as known for contact-induced reaching movements and spatial coordination of footfall patterns in stick insects" [77]. Integrating this concept into the SNN could synergize with the movement primitive neurons responsible for encoding phase transitions. For instance, these neurons might signal the optimal timing for the middle leg to transmit information to the ipsilateral hind leg, directing it to position its tarsus in proximity to the middle leg's current tarsus location. This would extend the network to include inter-leg coordination.

6 Conclusion

In conclusion, this thesis has successfully illustrated the feasibility of estimating the body pitch of a stick insect using distributed proprioceptive information through a SNN. The biological plausibility of the network corroborates the hypothesis that stick insects rely on proprioceptive cues to estimate body posture without the need for a dedicated organ. An existing SNN was modified and extended to simulate tactile hair proprioceptors, descending interneurons (joint angle/angular-velocity estimators), primitive interneurons (swing/stance classifiers), and posture neurons (body pitch estimation and a climbing classifier). Our findings suggest that the position interneuron performed with an error of approximately 5 % Gaussian noise relative to the ground truth, improved from 10 %. The velocity interneuron's classification increased in accuracy from 90.4 % to 9.29 % for a novel model and 95.6 % for a modified model. A key change is the ability to increase the firing rate up to four times. Primitive neurons were optimized to an average MCC of 0.56 and were found to efficiently encode for swing/stance or transition phases. The posture neuron estimated the body pitch with an average error of approximately 28 % Gaussian noise and the climbing classifier achieved an MCC of 0.59.

To further strengthen the hypothesis, introducing noise to the system, inherent in real biological neural circuits, could be explored. Additionally, expanding the dataset to include stick insects maneuvering around a pole would enable the study of movement-primitive neurons encoding natural turning, including yaw and pitch rotations. Moreover, exploring the potential for transition-signaling movement primitive neurons to assist in inter-leg coordination could provide insights into leg targeting influenced by neighboring legs.

This research holds potential applications in biomimetic robotics, where distributed proprioception could enhance substrate variability sensing and improve inclination estimates, with this thesis serving as a foundational reference. Overall, the findings outlined in this thesis contribute to our understanding of proprioceptive mechanisms in stick insects and pave the way for future investigations in this field.

References

[1] Norbert Wiener. *Cybernetics or Control and Communication in the Animal and the Machine*. MIT press, 2019.

[2] U Bässler. "Sensory control of leg movement in the stick insect Carausius morosus". In: *Biological cybernetics* 25.2 (1977), pp. 61–72.

[3] Chris J Dallmann et al. "A leg to stand on: Computational models of proprioception". In: *Current opinion in physiology* 22 (2021), p. 100426.

[4] Tibor I Tóth and Silvia Daun. "A kinematic model of stick-insect walking". In: *Physiological reports* 7.8 (2019), e14080.

[5] Volker Dürr, Josef Schmitz, and Holk Cruse. "Behaviour-based modelling of hexapod locomotion: linking biology and technical application". In: *Arthropod structure & development* 33.3 (2004), pp. 237–250.

[6] Akira Fukuhara et al. "Adaptive Interlimb Coordination Mechanism for Hexapod Locomotion Based on Active Load Sensing". In: *Frontiers in Neurorobotics* 16 (2022), p. 2.

[7] Jan M Ache and Volker Dürr. "Encoding of near-range spatial information by descending interneurons in the stick insect antennal mechanosensory pathway". In: *Journal of neurophysiology* 110.9 (2013), pp. 2099–2112.

[8] Nicholas S Szczecinski et al. "A computational model of insect campaniform sensilla predicts encoding of forces during walking". In: *Bioinspiration & Biomimetics* 16.6 (2021), p. 065001.

[9] Chris J Dallmann et al. "A load-based mechanism for inter-leg coordination in insects". In: *Proceedings of the Royal Society B: Biological Sciences* 284.1868 (2017), p. 20171755.

[10] Jan M Ache and Volker Dürr. "A computational model of a descending mechanosensory pathway involved in active tactile sensing". In: *PLoS computational biology* 11.7 (2015), e1004263.

[11] Arne Gollin and Volker Dürr. "Estimating body pitch from distributed proprioception in a hexapod". In: *Biomimetic and Biohybrid Systems: 7th International Conference, Living Machines 2018, Paris, France, July 17–20, 2018, Proceedings 7*. Springer. 2018, pp. 187–199.

[12] Yonatan Cohen. *Proprioceptive Encoding In Spiking Neural Networks*. Master's thesis. Bielefeld, Germany, Feb. 2020.

[13] Wolfgang Maass. "Networks of spiking neurons: the third generation of neural network models". In: *Neural networks* 10.9 (1997), pp. 1659–1671.

[14] Kashu Yamazaki et al. "Spiking neural networks and their applications: A Review". In: *Brain Sciences* 12.7 (2022), p. 863.

[15] J Okada and Y Toh. "Peripheral representation of antennal orientation by the scapal hair plate of the cockroach Periplaneta americana". In: *Journal of experimental biology* 204.24 (2001), pp. 4301–4309.

[16] Alex Schneider, Josef Schmitz, and Holk Cruse. "A bio-inspired joint controller for the decentral control of a closed kinematic chain consisting of elastic joints". In: *Proceedings of the 44th IEEE Conference on Decision and Control*. IEEE. 2005, pp. 233–238.

[17] John C Tuthill and Rachel Wilson. "Mechanosensation and Adaptive Motor Control in Insects". In: *Current Biology* 26 (Oct. 2016), R1022–R1038.

[18] Tatiana G Deliagina et al. "Neural bases of postural control". In: *Physiology* 21.3 (2006), pp. 216–225.

[19] MJ Cohen. "The response patterns of single receptors in the crustacean statocyst". In: *Proceedings of the Royal Society of London. Series B. Biological Sciences* 152.946 (1960), pp. 30–49.

[20] Michael L. Wiederhold, Christine E. Sheridan, and Nancy K. R. Smith. "Function of Molluscan Statocysts". In: *Origin, Evolution, and Modern Aspects of Biomineralization in Plants and Animals*. Ed. by Rex E. Crick. Boston, MA: Springer US, 1989, pp. 393–408. ISBN: 978-1-4757-6114-6.

[21] Jeremy M Wolfe et al. *Sensation & perception*. Sinauer Sunderland, MA, 2006.

[22] Azusa Kamikouchi et al. "The neural basis of Drosophila gravity-sensing and hearing". In: *Nature* 458 (Apr. 2009), pp. 165–71.

[23] Hubert Markl. "Borstenfelder an den Gelenken als Schweresinnesorgane bei Ameisen und anderen Hymenopteren". In: *Zeitschrift für vergleichende Physiologie* 45.5 (1962), pp. 475–569.

[24] John C Tuthill and Eiman Azim. "Proprioception". In: *Current Biology* 28.5 (2018), R194–R203.

[25] Uwe Proske and Simon C Gandevia. "The proprioceptive senses: their roles in signaling body shape, body position and movement, and muscle force". In: *Physiological reviews* (2012).

[26] Jeffrey Dean et al. "Control of walking in the stick insect: From behavior and physiology to modeling". In: *Autonomous Robots* 7 (1999), pp. 271–288.

[27] Ulrich Bässler and Ansgar Büschges. "Pattern generation for stick insect walking movements—multisensory control of a locomotor program". In: *Brain Research Reviews* 27.1 (1998), pp. 65–88. ISSN: 0165-0173.

[28] Sasha N Zill. "Plasticity and proprioception in insects I. Responses and cellular properties of individual receptors of the locust metathoracic femoral chordotonal organ". In: *Journal of experimental biology* 116.1 (1985), pp. 435–461.

[29] Laurence H. Field and Thomas Matheson. "Chordotonal Organs of Insects". In: ed. by P.D. Evans. Vol. 27. Advances in Insect Physiology. Academic Press, 1998, pp. 1–228.

[30] KM Chapman. "Campaniform sensilla on the tactile spines of the legs of the cockroach". In: *Journal of Experimental Biology* 42.2 (1965), pp. 191–203.

[31] André F. Krause, Andrea Winkler, and Volker Dürr. "Central drive and proprioceptive control of antennal movements in the walking stick insect". In: *Journal of Physiology-Paris* 107.1 (2013). Neuroethology, pp. 116–129. ISSN: 0928-4257.

[32] Angelique Paulk and Cole Gilbert. "Proprioceptive encoding of head position in the black soldier fly, Hermetia illucens (L.)(Stratiomyidae)". In: *Journal of experimental biology* 209.19 (2006), pp. 3913–3924.

[33] Holk Cruse. "The function of the legs in the free walking stick insect,Carausius morosus". In: *Journal of comparative physiology* 112 (1976), pp. 235–262.

[34] JWS Pringle. "Proprioception in insects: III. The function of the hair sensilla at the joints". In: *Journal of Experimental Biology* 15.4 (1938), pp. 467–473.

[35] Alfred Henry Sturtevant. *The north American species of Drosophila*. 301. Carnegie institution of Washington, 1921.

[36] Aloha Hannah-Alava. "Morphology and chaetotaxy of the legs of Drosophila melanogaster". In: *Journal of Morphology* 103.2 (1958), pp. 281–310.

[37] Ulrich Thurm. "An insect mechanoreceptor". In: *Cold Spring Harbor Symp. Quant. Biol.* Vol. 30. 1965, pp. 75–82.

[38] Malcolm Burrows. "The neurobiology of an insect brain". In: (1996).

[39] Holk Cruse, J Dean, and M Suilmann. "The contributions of diverse sense organs to the control of leg movement by a walking insect". In: *Journal of Comparative Physiology A* 154 (1984), pp. 695–705.

[40] Thomas Preuss and Roland Hengstenberg. "Structure and kinematics of the prosternal organs and their influence on head position in the blowfly Calliphora erythrocephala Meig." In: *Journal of Comparative Physiology A* 171 (1992), pp. 483–493.

[41] Mikko Juusola and Andrew S French. "Adaptation properties of two types of sensory neurons in a spider mechanoreceptor organ". In: *Journal of neurophysiology* 80.5 (1998), pp. 2781–2784.

[42] Philip L Newland et al. "The structure, response properties and development of a hair plate on the mesothoracic leg of the locust". In: *Journal of experimental biology* 198.11 (1995), pp. 2397–2404.

[43] Corinna Gebehart and Ansgar Büschges. "The processing of proprioceptive signals in distributed networks: insights from insect motor control". In: *Journal of Experimental Biology* 227.1 (2024).

[44] Michael Gebhardt and Hans-Willi Honegger. "Physiological characterisation of antennal mechanosensory descending interneurons in an insect (Gryllus bimaculatus, Gryllus campestris) brain". In: *Journal of Experimental Biology* 204.13 (2001), pp. 2265–2275.

[45] Akira Mamiya, Pralaksha Gurung, and John C Tuthill. "Neural coding of leg proprioception in Drosophila". In: *Neuron* 100.3 (2018), pp. 636–650.

[46] Charalampos Mantziaris, Till Bockemühl, and Ansgar Büschges. "Central pattern generating networks in insect locomotion". In: *Developmental neurobiology* 80.1-2 (2020), pp. 16–30.

[47] Géraldine von Uckermann. "Role of local premotor nonspiking interneurons in walking pattern generation of the stick insect Carausius morosus". PhD thesis. Universität zu Köln, 2008.

[48] Pavel E Musienko et al. "Activity of spinal interneurons during forward and backward locomotion". In: *Journal of Neuroscience* 42.17 (2022), pp. 3570–3586.

[49] HARALD Wolf and A Buschges. "Nonspiking local interneurons in insect leg motor control. II. Role of nonspiking local interneurons in the control of leg swing during walking". In: *Journal of neurophysiology* 73.5 (1995), pp. 1861–1875.

[50] Leslie M Theunissen, Holger H Bekemeier, and Volker Dürr. "Comparative whole-body kinematics of closely related insect species with different body morphology". In: *Journal of Experimental Biology* 218.3 (2015), pp. 340–352.

[51] Leslie M Theunissen and Volker Dürr. "Insects use two distinct classes of steps during unrestrained locomotion". In: *PLOS one* 8.12 (2013), e85321.

[52] Peter Dayan and Laurence F Abbott. *Theoretical neuroscience: computational and mathematical modeling of neural systems*. MIT press, 2005.

[53] Eugene M Izhikevich. "Which model to use for cortical spiking neurons?" In: *IEEE transactions on neural networks* 15.5 (2004), pp. 1063–1070.

[54] Romain Brette and Wulfram Gerstner. "Adaptive exponential integrate-and-fire model as an effective description of neuronal activity". In: *Journal of neurophysiology* 94.5 (2005), pp. 3637–3642.

[55] RJ Sayer, MJ Friedlander, and SJ Redman. "The time course and amplitude of EPSPs evoked at synapses between pairs of CA3/CA1 neurons in the hippocampal slice". In: *Journal of Neuroscience* 10.3 (1990), pp. 826–836.

[56] Larry F Abbott. "Lapicque's introduction of the integrate-and-fire model neuron (1907)". In: *Brain research bulletin* 50.5-6 (1999), pp. 303–304.

[57] Pavel Senin. "Dynamic time warping algorithm review". In: *Information and Computer Science Department University of Hawaii at Manoa Honolulu, USA* 855.1-23 (2008), p. 40.

[58] Gregory D Smith et al. "Fourier analysis of sinusoidally driven thalamocortical relay neurons and a minimal integrate-and-fire-or-burst model". In: *Journal of neurophysiology* 83.1 (2000), pp. 588–610.

[59] Rodolfo Llinás and Henrik Jahnsen. "Electrophysiology of mammalian thalamic neurones in vitro". In: *Nature* 297.5865 (1982), pp. 406–408.

[60] Alexander Robert Richard Casti et al. "A population study of integrate-and-fire-or-burst neurons". In: *Neural computation* 14.5 (2002), pp. 957–986.

[61] Seth Warner. *Modern algebra*. Courier Corporation, 1990.

[62] Brian W Matthews. "Comparison of the predicted and observed secondary structure of T4 phage lysozyme". In: *Biochimica et Biophysica Acta (BBA)-Protein Structure* 405.2 (1975), pp. 442–451.

[63] Davide Chicco and Giuseppe Jurman. "The advantages of the Matthews correlation coefficient (MCC) over F1 score and accuracy in binary classification evaluation". In: *BMC genomics* 21.1 (2020), pp. 1–13.

[64] David MW Powers. "Evaluation: from precision, recall and F-measure to ROC, informedness, markedness and correlation". In: *arXiv preprint arXiv:2010.16061* (2020).

[65] Holk Cruse et al. "Control of hexapod walking in biological systems". In: *Adaptive motion of animals and machines* (2006), pp. 17–29.

[66] Richard Naud et al. "Firing patterns in the adaptive exponential integrate-and-fire model". In: *Biological cybernetics* 99 (2008), pp. 335–347.

[67] Bernice D Mowery. "The paired t-test". In: *Pediatric nursing* 37.6 (2011), pp. 320–322.

[68] JWS Pringle. "Proprioception in insects: II. The action of the campaniform sensilla on the legs". In: *Journal of Experimental Biology* 15.1 (1938), pp. 114–131.

[69] Lay Kuan Loh and Mihovil Bartulovic. "Efficient coding hypothesis and an introduction to information theory". In: *Retrieved from users. ece. cmu. edu/˜ pgrover/teaching/files/InfoTheoryEfficientCo dingHypothesis. pdf. Homayoun Shahri* (2014).

[70] Jan M Ache, S Shuichi Haupt, and Volker Dürr. "A direct descending pathway informing locomotor networks about tactile sensor movement". In: *Journal of Neuroscience* 35.9 (2015), pp. 4081–4091.

[71] Tamar Flash and Binyamin Hochner. "Motor primitives in vertebrates and invertebrates". In: *Current opinion in neurobiology* 15.6 (2005), pp. 660–666.

[72] Stefan Schaal. "Dynamic movement primitives-a framework for motor control in humans and humanoid robotics". In: *Adaptive motion of animals and machines*. Springer, 2006, pp. 261–280.

[73] Holk Cruse. "Which parameters control the leg movement of a walking insect?: I. Velocity control during the stance phase". In: *Journal of Experimental Biology* 116.1 (1985), pp. 343–355.

[74] Holk Cruse. "Which parameters control the leg movement of a walking insect?: II. The start of the swing phase". In: *Journal of Experimental Biology* 116.1 (1985), pp. 357–362.

[75] Volker Dürr. "Stereotypic leg searching movements in the stick insect: kinematic analysis, behavioural context and simulation". In: *Journal of Experimental Biology* 204.9 (2001), pp. 1589–1604.

[76] A Aldo Faisal, Luc PJ Selen, and Daniel M Wolpert. "Noise in the nervous system". In: *Nature reviews neuroscience* 9.4 (2008), pp. 292–303.

[77] Volker Dürr and Malte Schilling. "Transfer of spatial contact information among limbs and the notion of peripersonal space in insects". In: *Frontiers in computational neuroscience* 12 (2018), p. 101.